

Chapter 4 Numerical Simulation of Large Scale Bottom Structure Grounding Experiment

4.1 Introduction

As discussed in Chapter 2, many research works on ship collisions and grounding using finite elements method have been published within the last decade. Although the modeling of the structure is quite laborious to set up and the simulation requires considerable hardware resources to perform, as numerical method and computer technology progress, it becomes relatively easier to simulate impacts on large and complicated structures. Today it is possible to simulate collisions and grounding involving large ship structures with thousands of degrees of freedom even at the PC level. Many powerful FEM codes that have been used for the simulation of ship collision and grounding are the explicit DYTRAN, RADIOSS, ABAQUS/Explicit, LS/DYNA3D, and the implicit NASTRAN, ABAQUS/Standard, ANSYS, MARC.

One of the pioneering studies involving finite-element simulations has been performed by Vredeveledt et al (1993). Those numerical simulations have considered the collision adequacy of inland vessels using MSC/Dytran. Some recent literature on numerical simulations of collision and grounding include Mizukami et al (1996), Kuroiwa (1996), Kitamura (1998, 2001), Servis & Samuelides (2000), Endo et al (2001), Wu et al. (2004).

Nonlinear finite element method (FEM) is a powerful tool for analyzing ship collision and grounding problems. The reliability of the numerical simulation results largely depends on the proper definition of problem and careful control of some critical parameters in FEM code. Servis et al (2002) attempted to determine the parameters that largely influence ship collisions in finite element code. Krzysztof et al (2003) studied the effect of parameters on crashworthiness of the struck ship by ABAQUS/Explicit code. The purpose of this chapter is to study the effect of selected parameters on crashworthiness of the single-hull bottom structure due to raking. The effect of the following parameters are considered: the boundary condition, the material model of the bottom structures, different shell element types, the friction coefficient for the contact between the bottom structures and the rock, the residual stress of the bottom structures.

In this chapter, numerical simulation of the bottom structures grounding experiment using nonlinear FE method is described qualitatively.

4.2 Bottom Structures Grounding Experiment of ASIS

The Association for Structural Improvement of the Shipbuilding Industry (ASIS 1993) carried out the static failure experiments of bottom structures due to bottom raking to examine the characteristic of the structural failure of oil tanker. A wedge-shaped rigid rock model which was fixed to a press machine was pushed against the bottom model along the direction of ship length quasi-statically. The single-hull bottom model with 1/3 scale of a VLCC bottom structure was tested. Figure 4.1 shows a schematic view of the experiments. The dimensions for rock model and single-hull bottom model are shown in Fig. 4.2 and Fig. 4.3. Figure 4.4 shows the stress-strain curves of different plates obtained from the tensile coupon test. Material property of different thickness plates is listed in Table 4.1. Six pictures taken during the experiment are shown in Fig. 4.5.

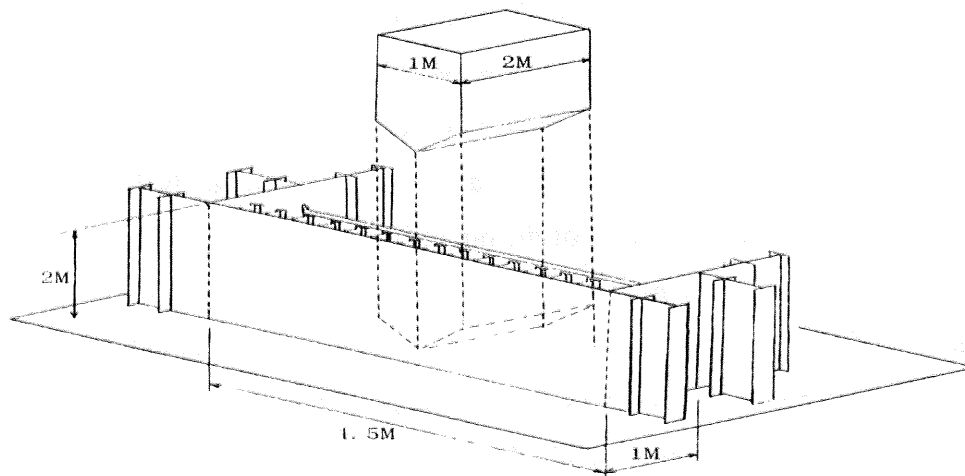


Fig. 4.1 Schematic view of the experiment

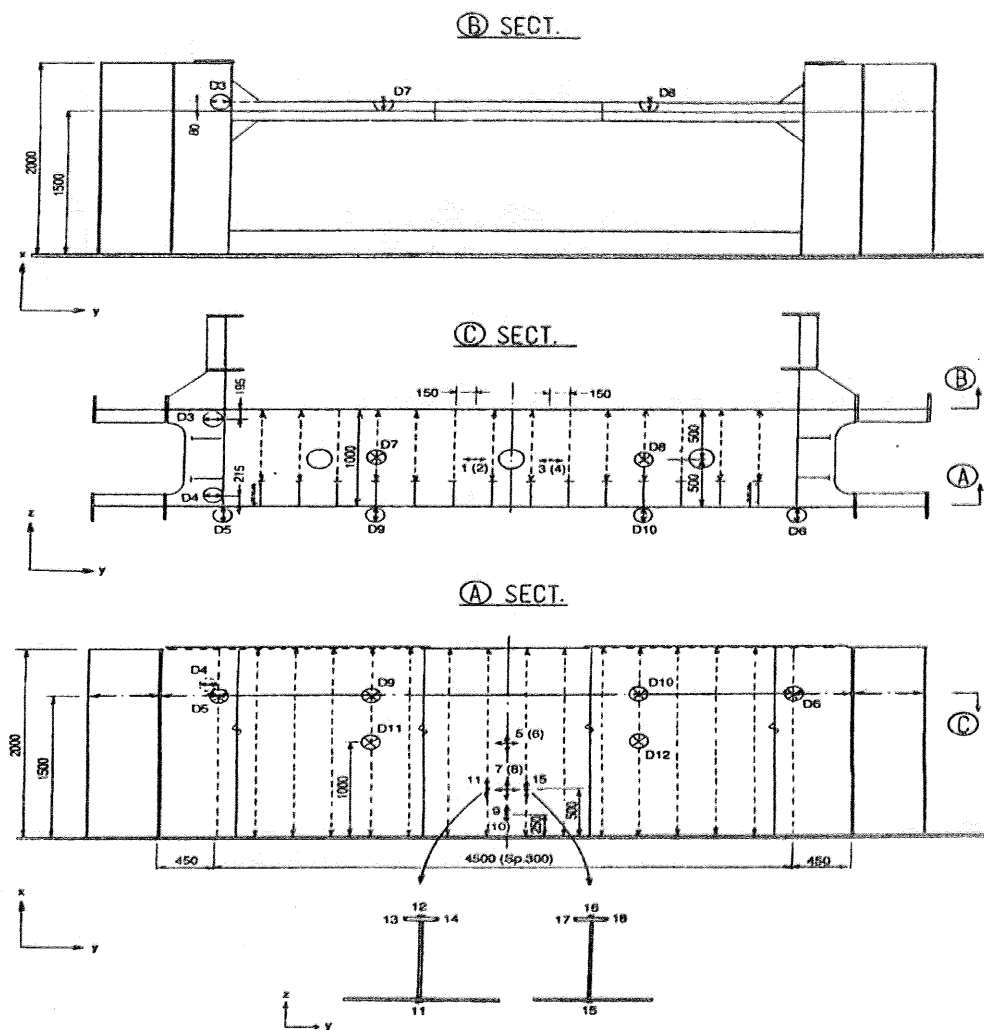


Fig. 4.2 Dimensions of single-hull bottom model

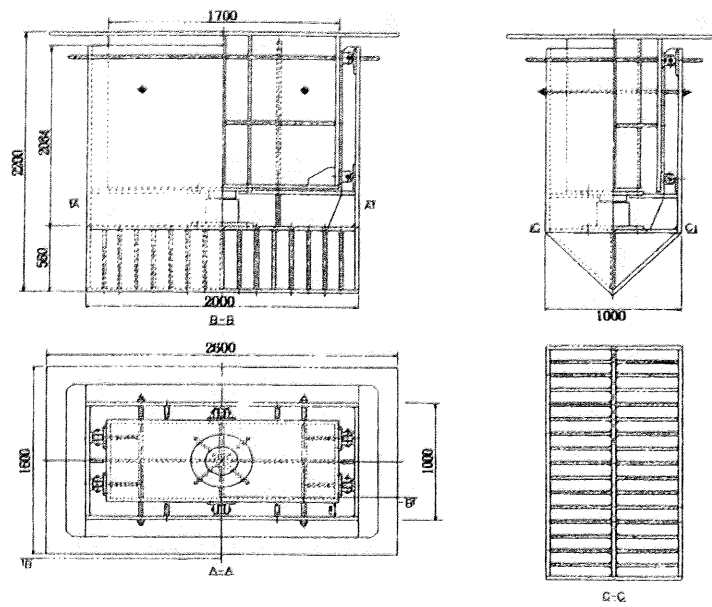


Fig. 4.3 Dimensions of rock model

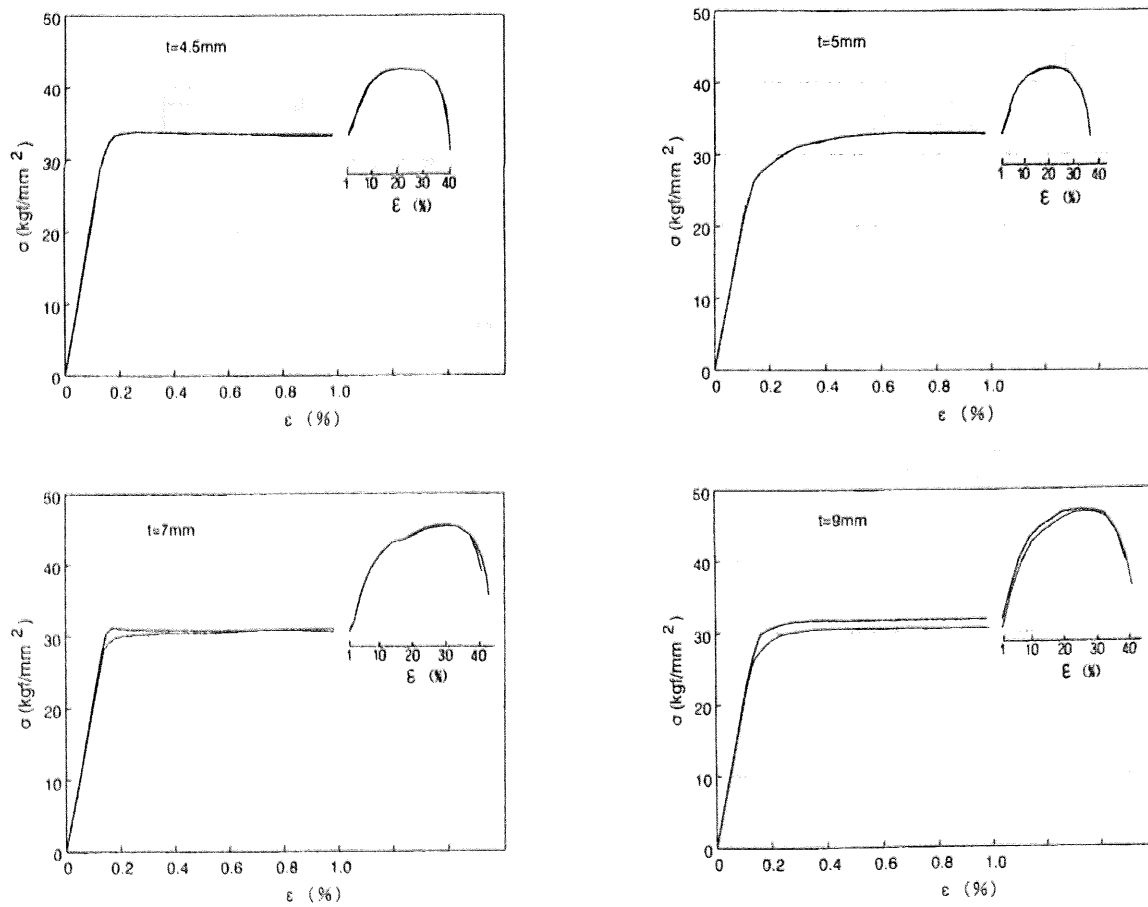


Fig. 4.4 Engineering stress-strain curves of different thickness plates

Table 4.1 Material property of different thickness plates

Thickness of plate (mm)	Yield Strength (MPa)	Ultimate Strength (MPa)	Rupture Strain	Young's Modulus (MPa)	Poisson Ratio
4.5	329.28	420.42	0.402	205800	0.3
5	310.66	412.58	0.399	205800	0.3
6	354.76	469.42	0.369	205800	0.3
7	306.74	446.88	0.412	205800	0.3
9	305.76	461.58	0.396	205800	0.3

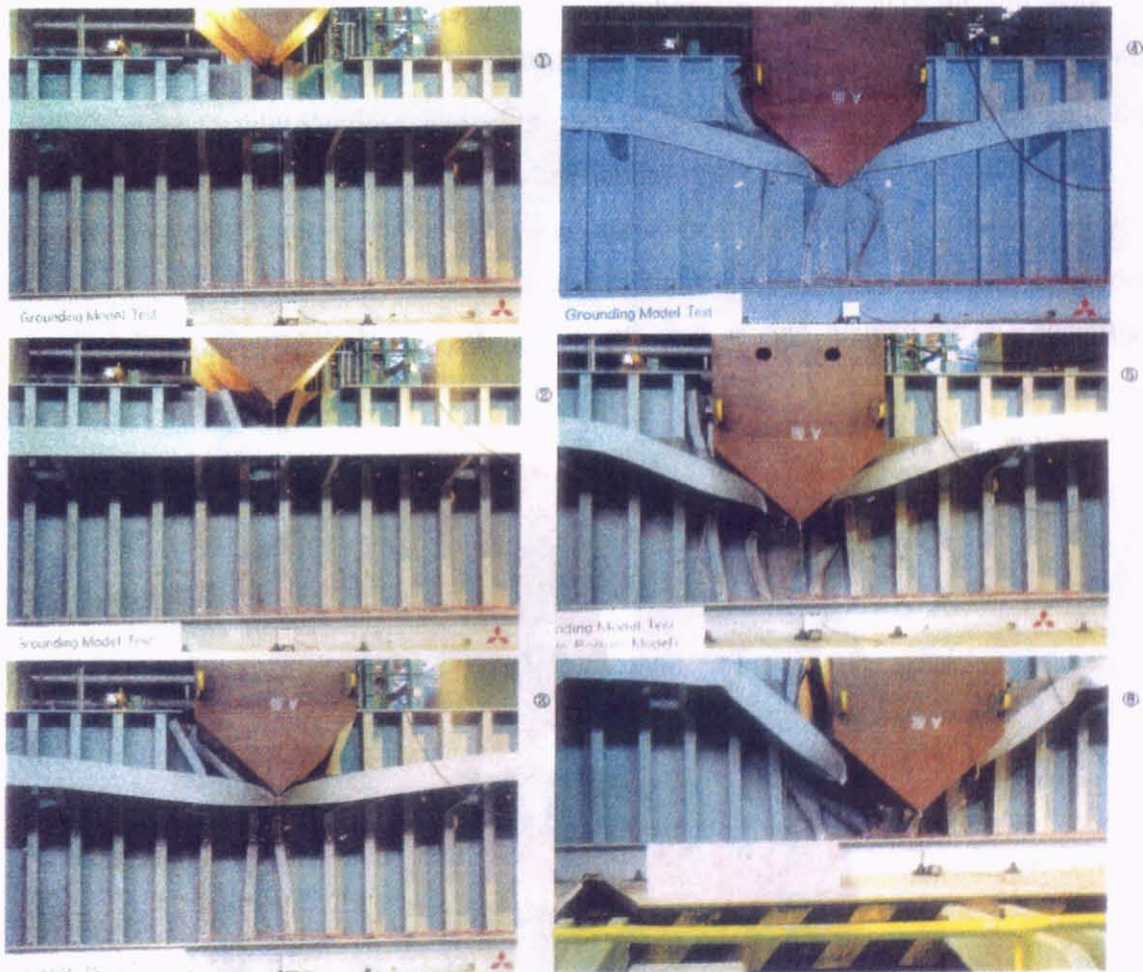


Fig. 4.5 Six pictures taken during the grounding experiment

4.3 Numerical Model

The single-hull bottom model is modeled as thin shell element and the mesh size is 20mm*20mm. The wedge-shaped rigid rock model is modeled as rigid body. Fig. 4.6 shows the meshed model of bottom structures.

The wedge-shaped rigid rock model was slowly pushed into bottom structures at a speed of 0.93mm/s in the experiment to reflect the quasi-static test condition. Through monitoring dynamic energy and ensuring that the majority of impact energy was dissipated in the deformed structures, attention in calculation was paid to the selection of rock model speed to achieve a reasonable balance between calculation accuracy and cost (CPU time).

Since the physical boundary condition was not explicitly modeled in the numerical simulation, two types of the boundary conditions were applied at the edge of bottom structures. This aspect will be discussed further in the next section of this chapter

The contact between the bottom model and the rock model and the contact between each part of the bottom structures were considered. The actual friction coefficient associated with the contacts was difficult to assess, therefore a parametric study for friction coefficient was performed. This aspect will also be discussed further in the next section of this chapter.

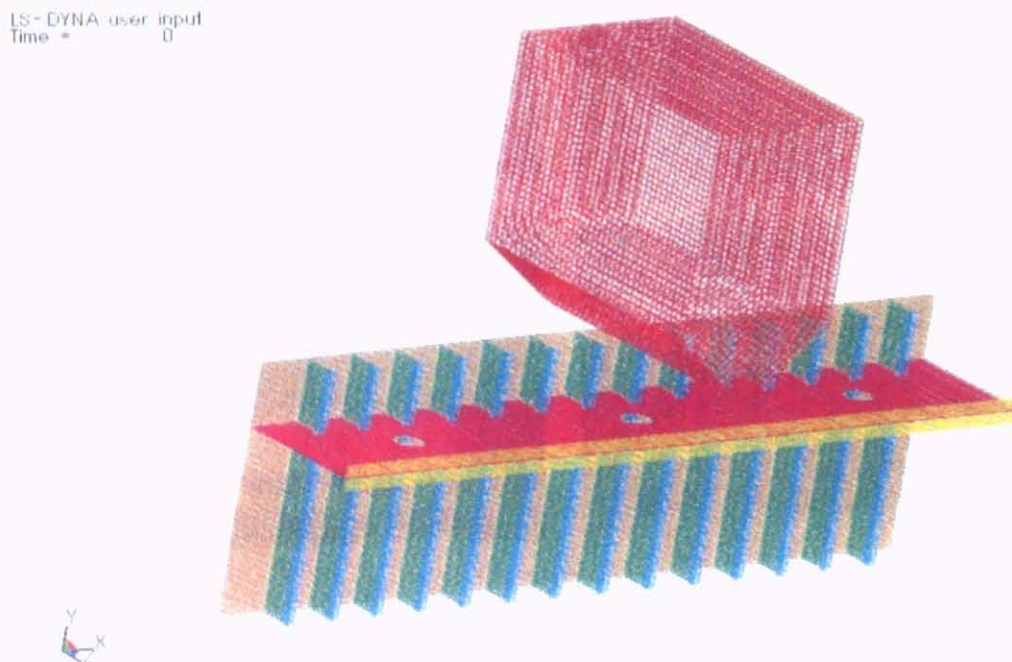


Fig. 4.6 Meshed model of bottom structures

Material failure was considered in the model using strain failure criterion. If the calculated effective plastic strain for any element exceeds the predefined value, the element will be removed from the model and the simulation continues with the eroded model.

There are 55,367 thin shell elements, 34,400 solid elements, 93,682 nodes and 562,092 degrees of freedom in FE model. The calculation time is about 46,154 seconds using personal computer (3 GHz CPU and 1.98 GB RAM). Fig. 4.7 shows the numerical simulation of deformation and failure of bottom structure. The impact force and absorbed energy curves are presented in Fig. 4.8.

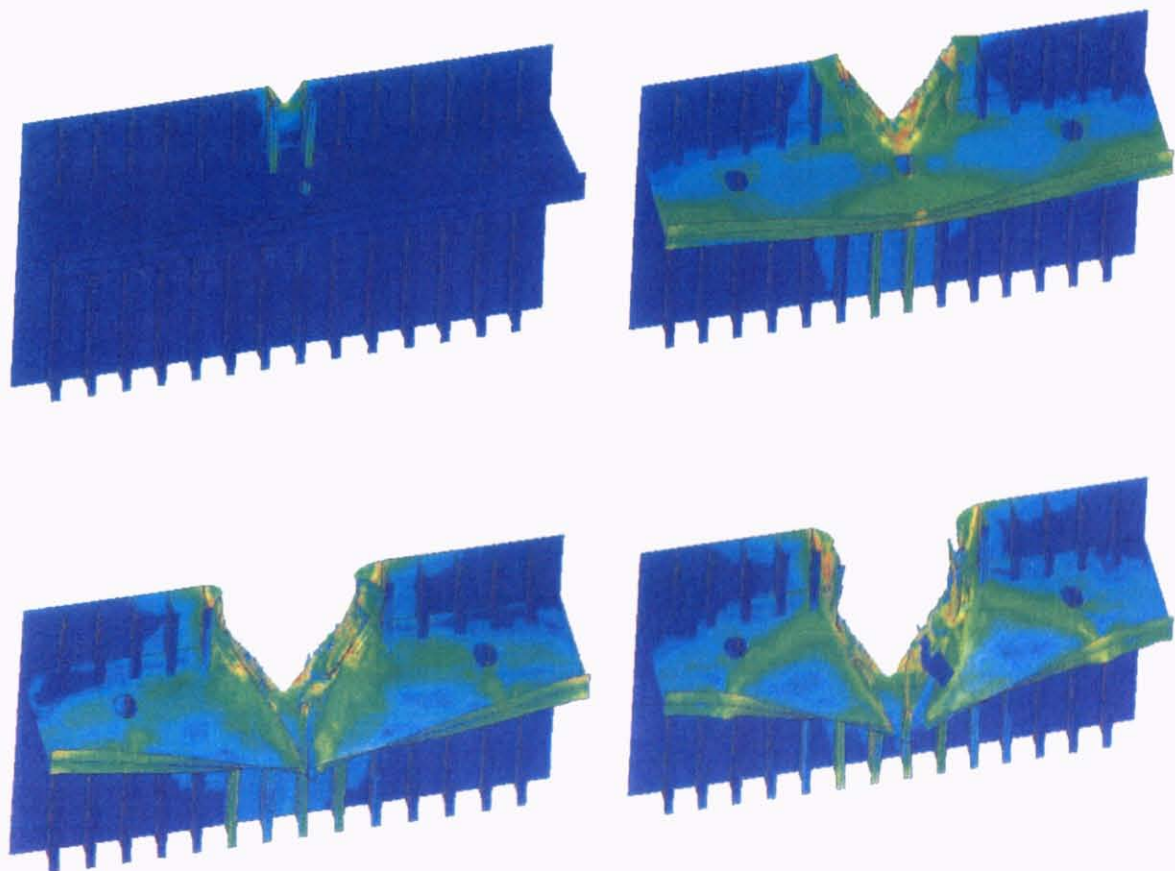


Fig. 4.7 Grounding process at the penetration depths of 150mm, 600mm, 1000mm and 1320mm respectively

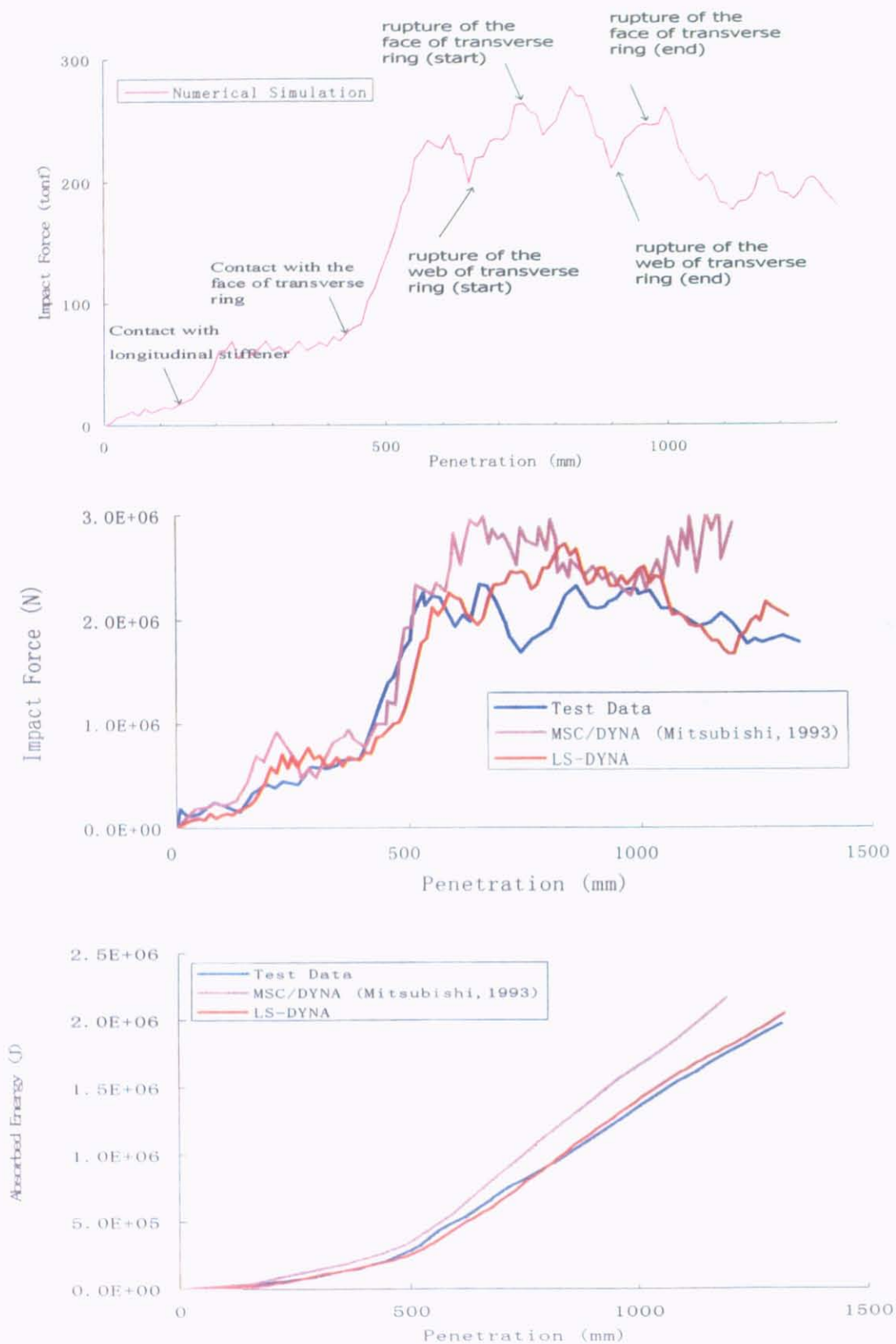


Fig. 4.8 Impact force and absorbed energy curves

4.4 Discussion of Selected Parameters

The effects of selected parameters are measured by comparing the different results in the impact force and absorbed energy vs. penetration of rock model, such as boundary condition, different shell element types, the residual stress of the bottom structures, the material model of the bottom structures, the friction coefficient for the contact between the bottom structures and the rock, the rupture strain of steel material

4.4.1 Effect of Boundary Condition

Since the physical boundary condition is not explicitly modeled in the numerical simulation, two types of the boundary conditions are applied at the right, left and bottom edges of bottom structures (see Fig. 4.9):

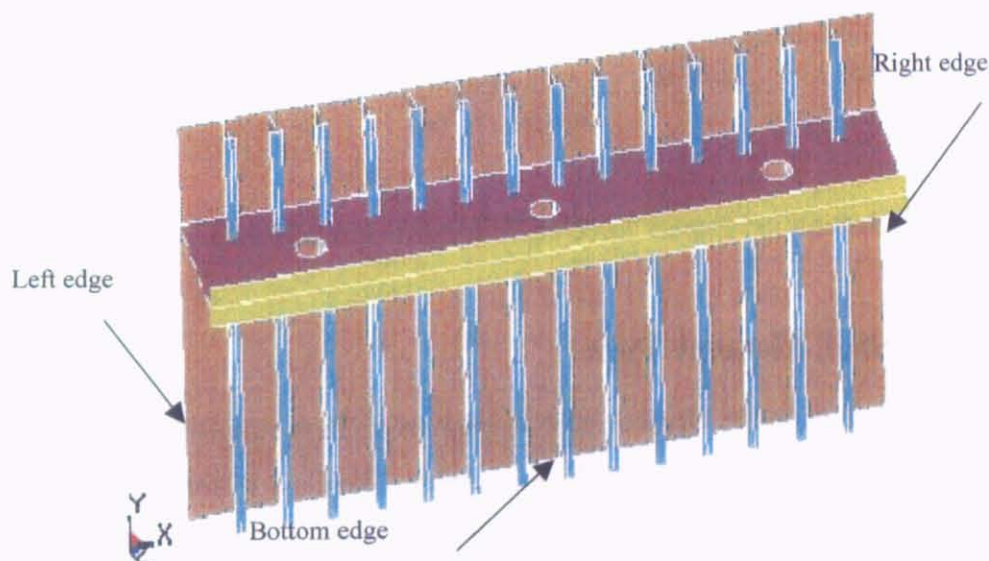


Fig. 4.9 Boundary condition of FE model

- BC1 All displacements and rotations were suppressed
- BC2 All displacements were suppressed

To study the effect of boundary condition, the same values of the other parameters are used. Fig. 4.10 shows the force-penetration curves for different boundary conditions BC1 and BC2. We can see that the difference between the force-penetration curves for BC1 and BC2 is much smaller. There is a difference of 1.8% in the maximum impact forces between

BC1 and BC2. The obtained results indicated that the impact force is insensitive to the boundary condition type. We suppose that the supports for the bottom structures in the experiments were rigid enough. In the following numerical model, all displacements and rotations at the edge of bottom structures were restricted.

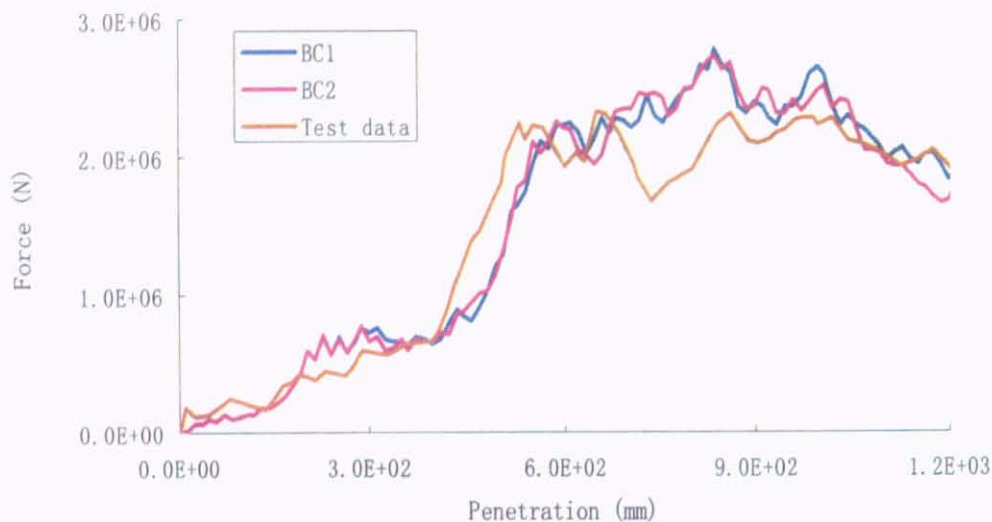


Fig. 4.10 Penetration-impact force curve for different boundary conditions

4.4.2 Effect of Shell Element Type

Shell elements are the main element type in crashworthiness simulations and possible to simulate complex structure failure with high accuracy. There are different kinds of shell elements available in nonlinear finite element program for modeling ship structures in order to perform nonlinear impact analyses.

Belytschko-Tsay (BT) shell element as a computationally efficient has become the default shell element formulation in nonlinear FE code LS-DYNA. Since BT shell element is based on a perfectly flat geometry, warpage is not considered. The effect of neglecting warpage in bottom model grounding experiment cannot be predicted beforehand and may lead to less than accurate results, but the latter is difficult to verify in practice. Belytschko-Wong-Chiang (BWC) shell element can consider the warping stiffness with reasonable added computational cost.

Belytschko-Tsay shell element and Belytschko-Wong-Chiang shell element are applied in numerical simulation respectively. The effect of shell element type on penetration-force curve is shown in Fig. 4.11. The obtained results indicate that the difference of penetration-impact force curves between BT shell element and BWC shell element is much smaller. However the calculation time increases approximately 40% using BWC shell element instead of BT shell element. If adequate mesh size is applied, good predicted result can be obtained for nonlinear impact analysis using BT shell element. In the following numerical model, BT shell elements are used.

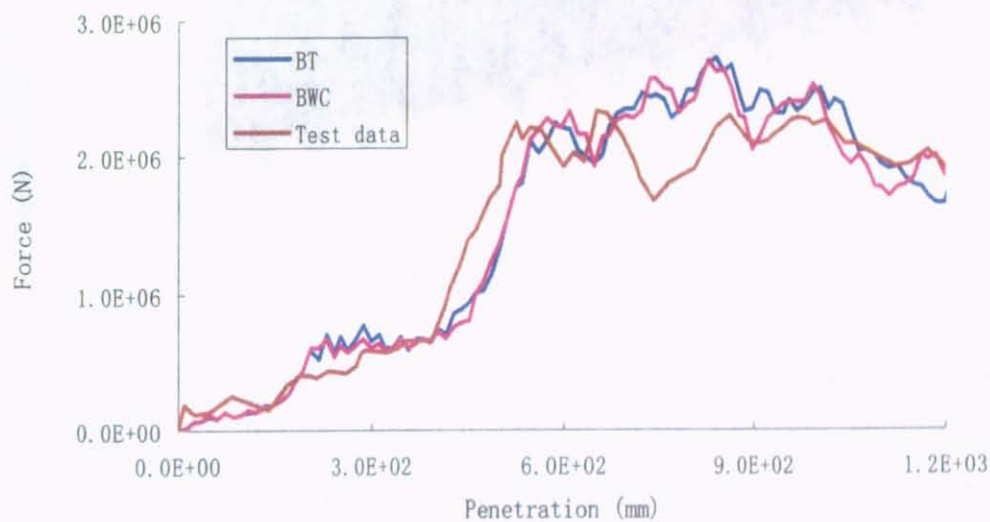


Fig. 4.11 Impact force and absorbed energy curves for different element types

4.4.3 Effect of Residual Stress

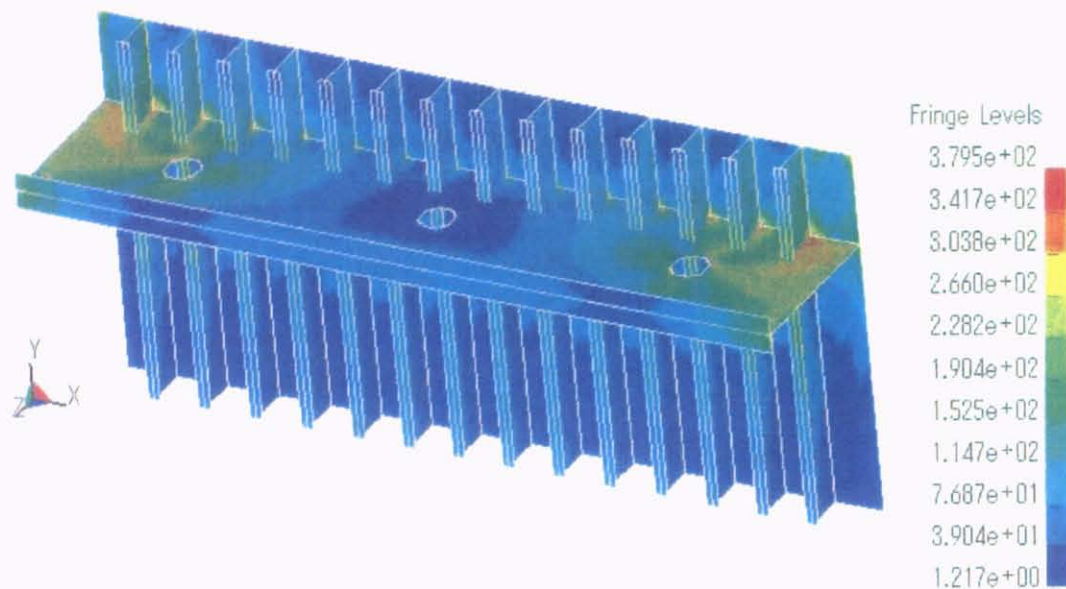


Fig. 4.12 Impact force and absorbed energy curves for different element types

Since geometric imperfections and welding in the bottom structures will induce the residual stress, the effect of residual stress on the impact force is investigated. The residual stress had been calculated by moving the upper edge nodes of bottom structure about 6mm and 12mm in horizontal direction while the nodes of other three ends are restricted, respectively. The residual stress of the bottom structure with 6mm initial imperfection is shown in Fig. 4.12. In this exercise, the residual stress caused by initial geometric imperfections is considered simply.

The bottom structure is exposed to the global tension in longitudinal direction(y axis). Then FE analysis is conducted using pre-estimated residual stress as the initial stress. Histories of impact force and absorbed energy is shown in Fig. 4.13 as well as the result of without residual stress. The difference among the three curves is much less. When the penetration is in the range from 0mm to 600mm, the curve of 6mm initial imperfection and the curve of 12mm initial imperfection are the same curve. Those two curves also have the same maximum impact force at the same location of penetration. The maximum impact force has increased 10.6% when the residual tensional stress is applied.

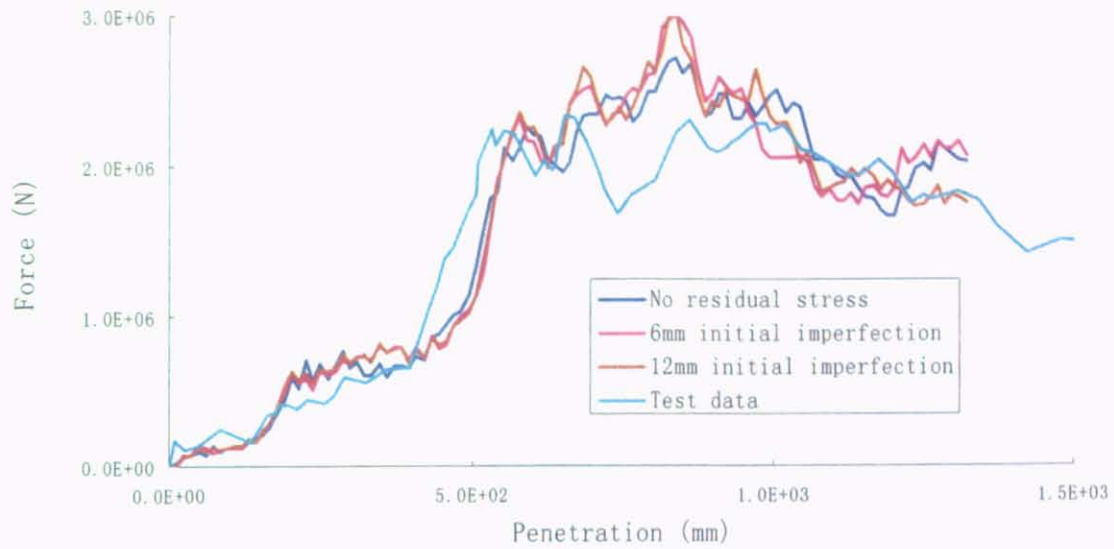


Fig. 4.13 Impact force and absorbed energy curves for different initial imperfections

Kitamura (2001) performed several large-scale finite element simulations of ship-ship collisions coupling ship collision and horizontal hull girder bending. He showed that the smaller contact area result in the slight effect of residual stress on the impact force. Since the contact area is relatively small in the grounding experiment, the effect of residual stress on the impact force may be limited in general. In the following numerical model, the residual stress is not considered.

4.4.4 Effect of Material Model

Since the bottom structure grounding experiment involves extreme structural behaviors with both geometrical and material nonlinear effects, the input of material properties up to the ultimate tensile stress has a significant influence on the extent of absorbed energy of bottom structure. It is noted that the true stress-strain characteristics of the material are required in the nonlinear finite element code LS-DYNA. The true stress and strain are related to engineering (or nominal) stress and strain as follows:

$$\sigma_{true} = \sigma_{eng} (1 + \varepsilon_{eng}), \quad \varepsilon_{true} = \ln(1 + \varepsilon_{eng}) \quad (4.1)$$

In most case, only limited material properties are available on the test setup. In generally, the material model is defined as an elastic-perfectly plastic material model

(Mat.1). The true stress-strain curve based on the ultimate stress and the failure strain (Zhang 2004) is given in the following way (Mat.2).

$$\sigma = C \cdot \varepsilon^n \quad (4.2)$$

$$n = \ln(1 + \varepsilon_f) \quad (4.3)$$

$$C = \sigma_u \left(\frac{e}{n} \right)^n \quad (4.4)$$

where

ε_f : the rupture strain; σ_u : the ultimate stress;

e : the natural logarithmic constant

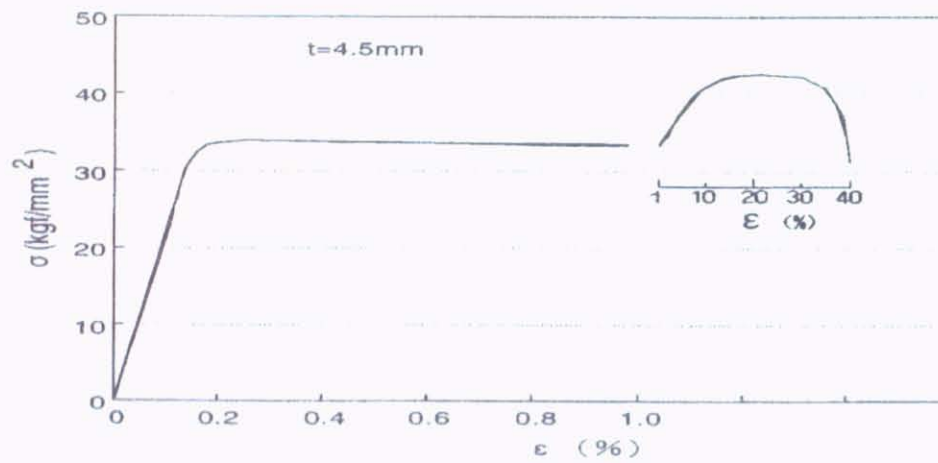


Fig. 4.14 Engineering stress-strain curve for 4.5mm thickness plate

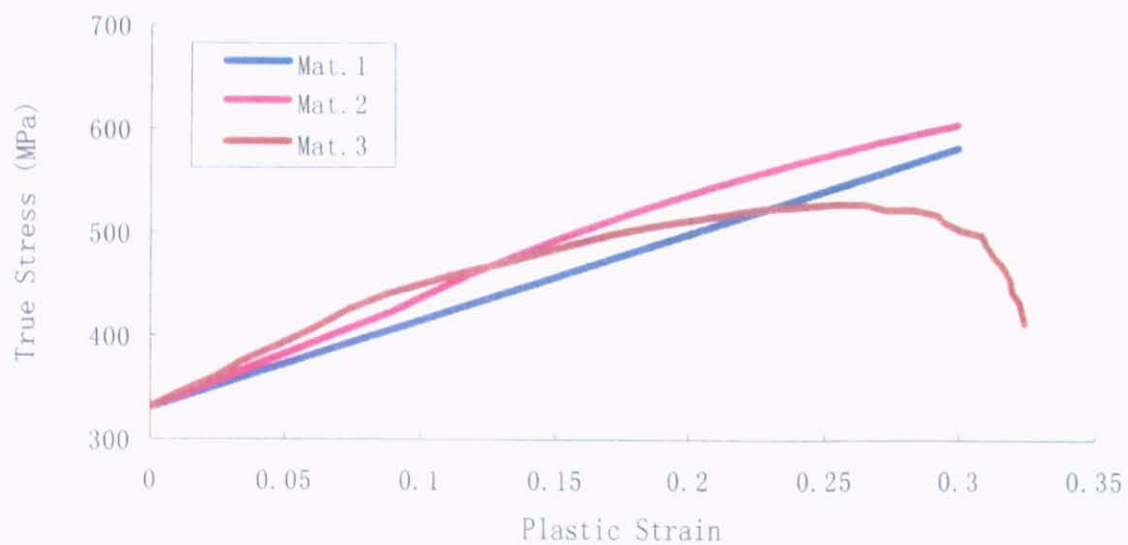


Fig. 4.15 True stress-plastic strain curves for 4.5mm thickness plate

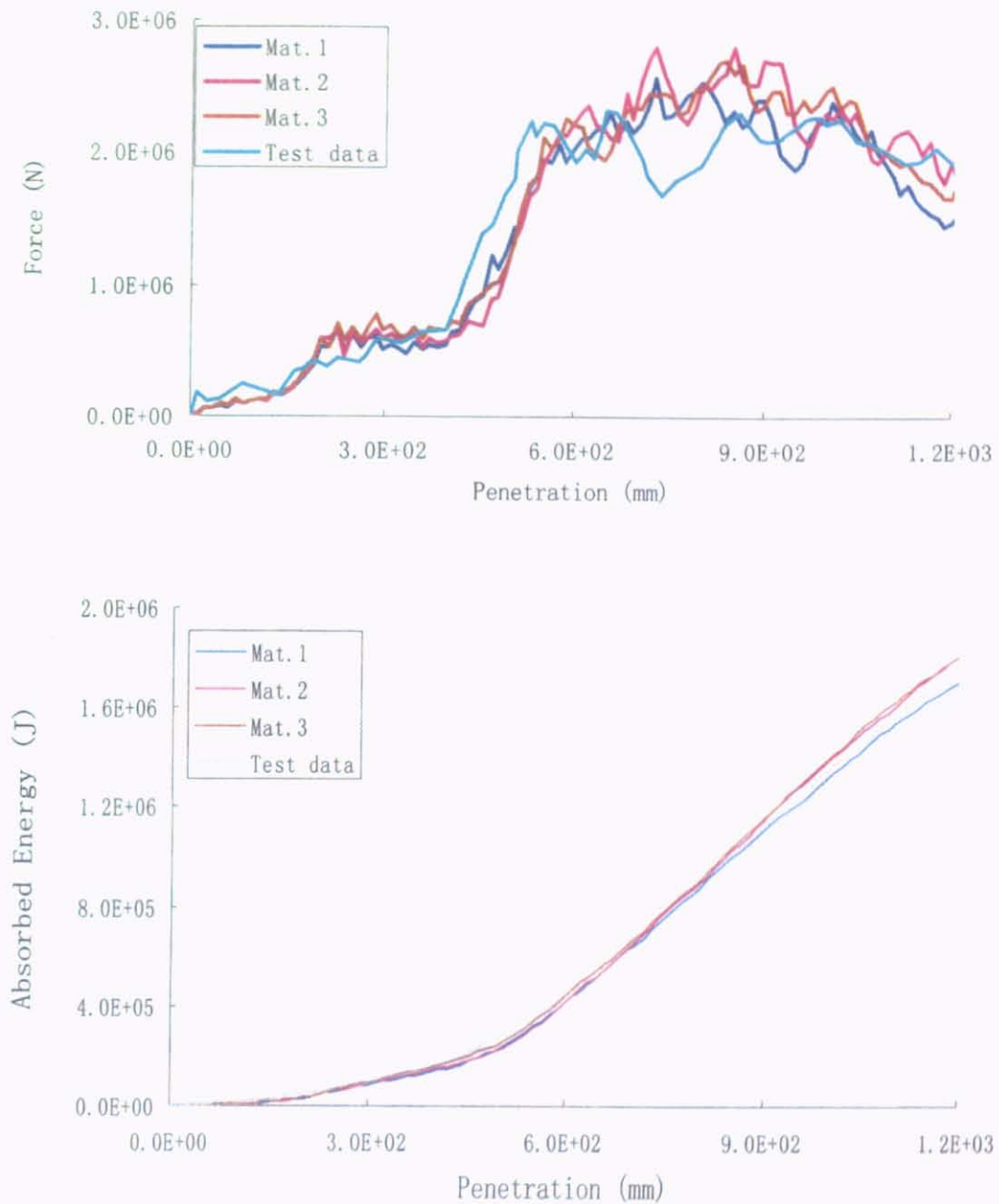


Fig. 4.16 Impact force and absorbed energy curves for different material models

If the tensile coupon tests of plates were conducted, the stress-strain curve obtained from the experiment can be used in numerical simulation (Mat.3). Fig. 4.14 shows the stress-strain curve of the 4.5mm thickness plate obtained from the tensile coupon test. Three types of true stress-plastic strain curves of 4.5mm plate are shown in Fig. 4.15.

The effect of material types on the histories of impact force and absorbed energy is shown in Fig. 4.16. Since both the strain-hardening and necking effects are not taken into account in material model 1, it results in lower impact force and lower energy absorption capacity. Numerical results of material model 2 and 3 have the same penetration- absorbed energy curves. In numerical simulation, if only limited material properties are available, the material model 2 is recommended and good prediction of impact force and absorbed energy curve can be obtained. In the follow numerical simulation, the material model 2 is used.

4.4.5 Effect of Friction Coefficient

In numerical simulation, contact between the bottom model and the rock model and contact between each part of the bottom structures need to be considered. However the actual friction coefficient associated with the contacts is difficult to assess. According to LS-DYNA user manual, under normal dry surface condition, the friction coefficient on mild-steel-on-mild-steel surface is 0.74 for static friction and 0.57 for sliding friction. In engineering practice, both the static and dynamic friction coefficients equal 0.3 is used in most case and the value of friction coefficient larger than 0.6 is rarely used. Therefore it is necessary to perform a parametric study for friction coefficient. The values of friction coefficient equal 0.0, 0.1, 0.2, 0.3, 0.4, 0.5 and 0.6 are applied for parametric study. To study the effect of friction coefficient, the same values of the other parameters were used.

Figure 4.17 shows that the impact force increases as the friction coefficient increases. In comparison with the case without friction, the impact force significantly increases when the friction coefficient equal 0.6 is applied. The maximum impact force increases approximately 60% while the friction coefficient increases from 0 to 0.6. We can also see that the difference between the curves for 0.3 and 0.6 is much less than the difference between the curves for 0.0 and 0.3.

The friction coefficient has significant influence on the history of impact force when it is in the range from 0 to 0.3. The impact force becomes insensitive to the friction coefficient when it increases from 0.3 to 0.6. We can except that the effect of the friction coefficient on impact force will not become remarkable when the value of friction coefficient larger than 0.6.

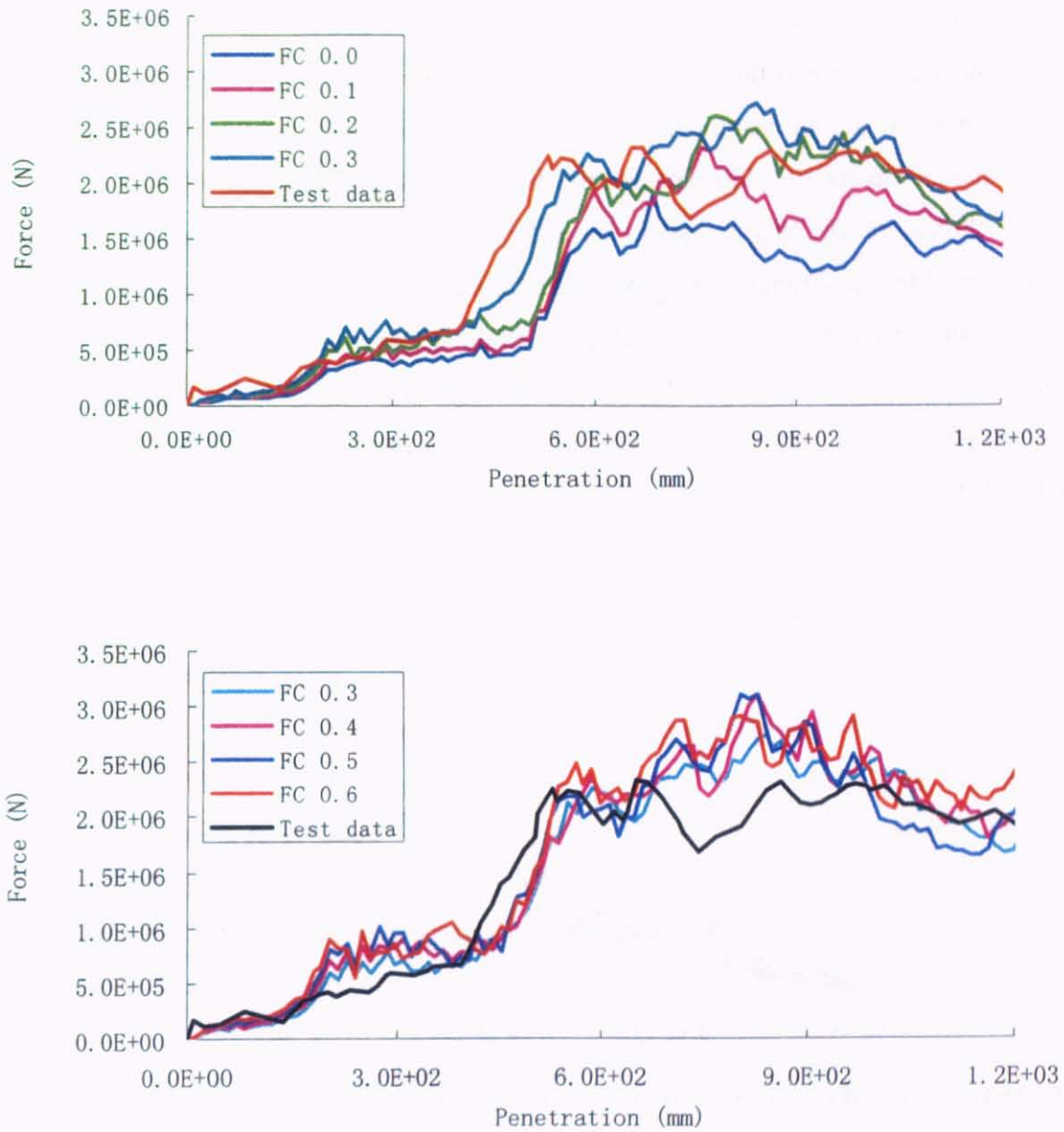


Fig. 4.17 Impact force and absorbed energy curves for different friction coefficients

4.4.6 Effect of Rupture Strain

A major challenge in numerical simulation of ship collision and grounding is the prediction and simulation of initiation and propagation of fracture. The most commonly used assumption is that fracture occurs when the equivalent strain reaches a critical value.

If the calculated strain, such as plastic effective strain and principal strain, exceeds its defined rupture strain values, the element will be fractured and deleted from the FE model. Due to the local nature of the fracture initiation and propagation, the rupture strain value to be used in FE model are mesh dependent. ISSC collision and grounding committee (ISSC 2003) studied the relationship between the rupture strain and element size and proposed proper curves for the rupture strain as a function of the element size by numerical simulation of tensile coupon test of mild steel. Since FE model of the large ship structures is always the coarse mesh, the defined rupture strain values is given to the nominal fracture strain values obtained by material coupon test in general. In this case, different rupture strains of the face of transverse ring are used to investigate its influence on the history of the force-penetration curve.

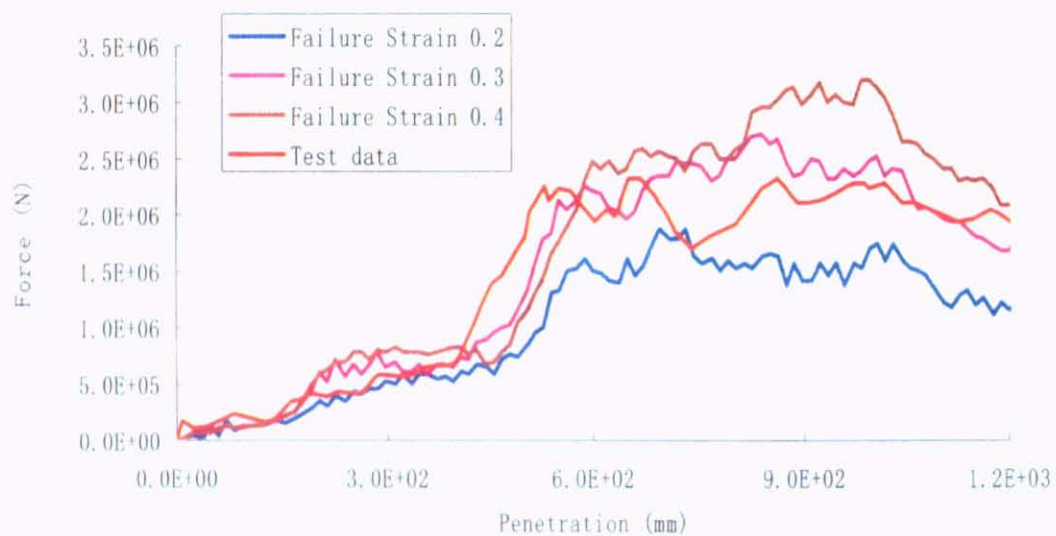


Fig. 4.18 Impact force curve for different rupture strains

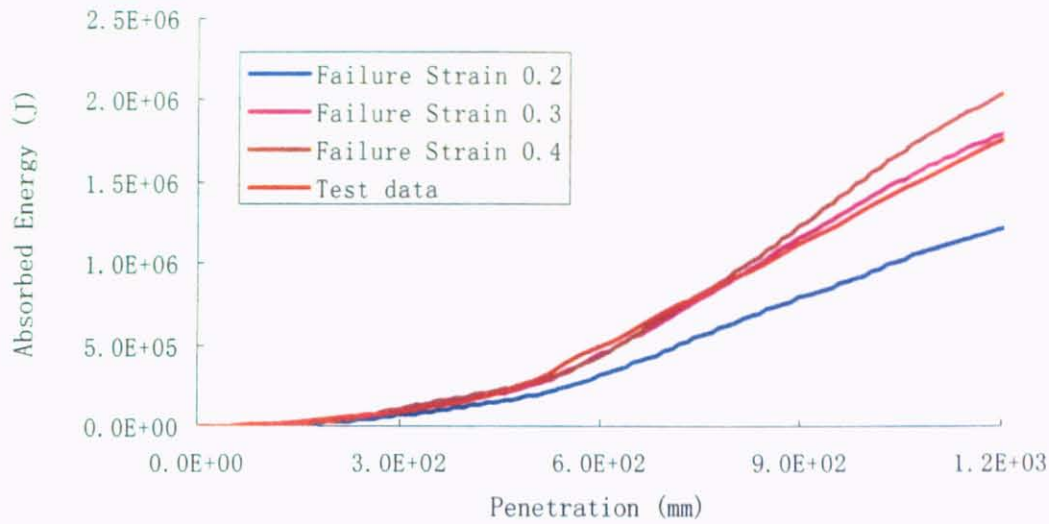


Fig. 4.19 Absorbed energy curve for different rupture strains

Fig. 4.18 and 4.19 illustrate the impact force and the absorbed energy with different rupture strain values of 20%, 30% and 40% respectively. Calculation results show that the absorbed energy curves respond very sensitively to the defined rupture strain. It is shown that the definition of the rupture strain value is a most important key point for a correct prediction of force and absorbed energy curve. Lower rupture strain results in lower resistance and lower energy absorption capacity. In this case, we find that a 50% reduction of rupture strain (from 0.4 to 0.2) causes 40.36% reduction of energy absorption capacity near the 1200mm penetration.

4.4.7 Effect of Interaction between Friction Coefficient and Rupture Strain

As mentioned above, the friction coefficient and the rupture strain are two important key parameters in the influence of numerical simulation of ship grounding. It is necessary to study the absorbed energy of the bottom structure as a function of the friction coefficient and the rupture strain. In this case, the friction coefficient varies from 0.2 to 0.5 and the rupture strain of the face of transverse ring varies from 20% to 40% are run to investigate this relationship by numerical simulation.

Table 4.2 Numerical results of absorbed energy at end of face of transverse ring rupture with different friction coefficient and rupture strain

Absorbed Energy(KJ)		Friction Coefficient			
		0.2	0.3	0.4	0.5
Rupture Strain	0.2	795.3	957.5	1017.9	1077.5
	0.3	1272.4	1418.7	1461.3	1524.9
	0.4	1459.3	1567.8	1715.3	1778.7
Test data		1365.9			

Table 4.2 gives the absorbed energy at end of face of transverse ring rupture with different friction coefficient and rupture strain. Fig.4.20 shows the surface of the dimensional absorbed energy with different friction coefficient and rupture strain. It is interesting to find that the surface is an approximate plane. Based on dimensional analysis and applying a least-square best fit to the numerical data, the absorbed energy as a function of the friction coefficient and the rupture strain can be expressed as follows:

$$\frac{E_{Num}}{E_{Test}} = f(\mu, \varepsilon_f) = 0.6867\mu + 2.4450\varepsilon_f + 0.0052 \quad (4.5)$$

where

E_{Num} : the numerical simulation result of absorbed energy

E_{Test} : the test data of absorbed energy

μ : the friction coefficient

ε_f : the rupture strain.

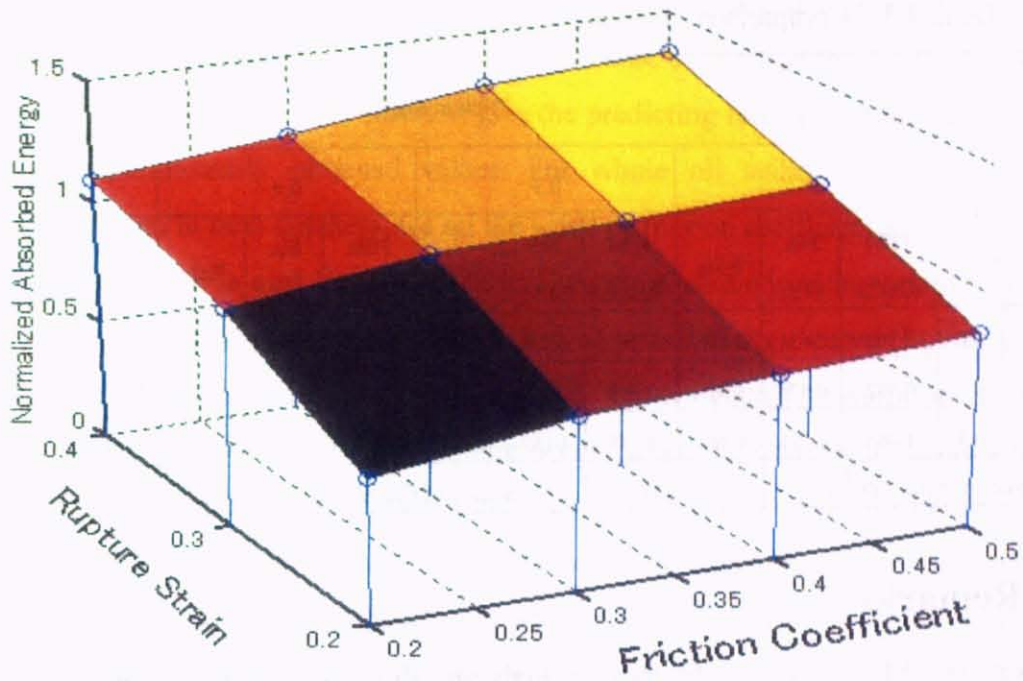


Fig. 4.20 Surface of the dimensional absorbed energy

It is shown that the absorbed energy increases linearly with the friction coefficient and the rupture strain in the equation (4.5). The table 4.3 shows the numerical simulation results and the predicted absorbed energy by equation (4.5).

The square of the error of a linear regression of μ_i, ε_{fi} on f_i by the equation (4.5)

$$\sigma_{f|\mu, \varepsilon_f}^2 = \frac{1}{n-1} \sum_{i=1}^n (f_i - 0.6867\mu - 2.445\varepsilon_f - 0.0052)^2 = 0.0024 \quad (4.6)$$

The square of the correlation coefficient

$$R^2 = 1 - \frac{\sigma_{f|\mu, \varepsilon_f}^2}{\sigma_f^2} = 0.954 \quad (4.7)$$

So we can say that the prediction results using equation (4.5) compare well with the numerical simulation results.

Table 4.3 Comparison of equation (4.5) with the numerical simulation results

Dimensionless Absorbed Energy		Friction Coefficient											
		0.2			0.3			0.4			0.5		
		FEM Results	Eqs. (4.5)	Error	FEM Results	Eqs. (4.5)	Error	FEM Results	Eqs. (4.5)	Error	FEM Results	Eqs. (4.5)	Error
Rupture Strain	0.2	0.582	0.631	8.47%	0.701	0.700	0.11%	0.745	0.769	3.17%	0.789	0.838	6.17%
	0.3	0.932	0.876	5.96%	1.039	0.945	9.04%	1.070	1.014	5.28%	1.116	1.082	3.08%
	0.4	1.068	1.121	4.88%	1.148	1.189	3.61%	1.256	1.258	0.16%	1.302	1.327	1.87%
Square of Error (σ^2)				0.0024		Square of Correlation Coefficient (R^2)						0.954	

4.5 Remarks

Nonlinear FEM is a powerful tool for analyzing ship collision and grounding problems. However, the reliability of the numerical simulation results largely depends on the proper definition of problem and careful control of some critical parameters in FEM code. The purpose of this chapter is to study the effect of selected parameters on crashworthiness of the single-hull bottom structure and propose some guidelines for whole oil tanker collision numerical simulation in next chapters.

- 1) **Shell element type:** FE model using Belytschko-Tsay shell element, which is assumed to be perfectly flat, also can give good predicted result and capture the main failure modes for high nonlinear impact analysis as well as low CPU time if adequate mesh size is applied. Belytschko-Tsay shell element is widely used shell element type in oil tanker collision numerical analyses.
- 2) **Material model:** If only limited material properties (the ultimate stress and the engineering failure strain) are available, we can use equations (4.2)-(4.4) to obtain the true stress-strain curve (material model 2). Using material model 2, good predicted result on impact force and absorbed energy can be obtained. The material model 2 is recommended and applied to oil tanker collision simulation in next chapters
- 3) **Friction coefficient:** It is difficult to assess the actual value of friction coefficient, therefore a parametric study was performed. When the value of friction coefficient is in the range from 0 to 0.3, it significantly influences on the history of impact

force. On the other hand, its influence becomes insensitive when the value of friction coefficient is more than 0.3. The value of the friction coefficient, which has been selected as 0.3, seems to give the predicting force-penetration curve close to experimentally obtained values. For whole oil tanker collision numerical simulation in next chapters, we set the value of friction coefficient as 0.3.

- 4) **Failure criteria and Rupture strain:** The rupture strain is an important parameter for an accurate prediction of force and absorbed energy curve. Lower rupture strain results in lower resistance and lower energy absorption capacity. Traditionally, we assume that rupture occurs when the equivalent plastic strain in an analyzed structure reaches a critical value. This critical value of rupture strain is related to the strain-stress curves obtained from mechanical tests of uniaxially stretched metal coupons. Such value seems to result in realistic failure modes and reasonable load-carrying capacity of structure. For whole oil tanker collision numerical simulation in next chapters, the critical rupture strain is used to simulate the initiation and propagation of fracture.

Chapter 5 Numerical Simulation of Fluid-structure Interaction of Liquid-filled Cargo Tank during Ship Collision

5.1 Introduction

Ships carrying liquid cargo sometimes unavoidably were struck by other vessels. In ship collision and grounding accidents, outflow of hazardous cargoes such as crude oil will cause very serious consequences for the environment, the human lives and the property. It is necessary to evaluate fluid-structure interaction of liquid cargo filled tank during ship collision and grounding.

For fluid-structure interaction problems, the main problem of numerical calculation is that the deformation of the fluid mesh near the structure undergoes largely and the time step becomes very small for explicit calculations. The Arbitrary Lagrangian Eulerian (ALE) finite element method is able to create a new undistorted mesh for fluid domain and allow the calculation to continue. The ALE finite element method solves the transient equations of motion of the fluid and structure using the explicit time integration method. Fluid/structure coupling calculations are carried out each time step. This method is suitable to analyze highly dynamic, highly nonlinear phenomena lasting for short time such as the impact of the fluid on tank during ship collision.

The Lagrangian finite element approach is also an effective tool for the analysis of the flow of fluid. Using the Lagrangian approach to describe the flow of fluid, the mesh follows the material. The interaction between fluid and structure was modelled using the contact algorithm.

Tabri et al. (2004) has revealed that the fluid-structure interaction on the unfilled tank has a remarkable effect on the motion and structural response of the struck ship in collision. In that paper, the fluid-structure interaction in the ballast tank is treated as liquid sloshing and the effect of sloshing is modelled as equivalent linear mass-spring model. More accurately, the sloshing effect is modelled by splitting the fluid mass into a part rigidly connected to the structure and the rest mass connected via a spring.

In section 5.2, the ALE finite element method is validated by the rectangular tank sloshing experiment (Pierre C. Sames et al 2002). Numerical simulation procedure of the ship collision between a 72,000 tonne oil tanker collide with the crude oil cargo tanker of a 293,000 tonne double hull VLCC taking account of fluid-structure interaction is presented. Four different numerical models were adopted to model fluid-structure interaction in liquid

filled cargo tank, namely Arbitrary Lagrangian Eulerian model, Lagrangian FE model, Linear Sloshing model and Rigid Point Mass model.

5.2 Validation of ALE FE Method on the Rectangular Tank Sloshing Experiment

To check the validation of ALE finite element method outlined above in fluid-structure interaction, two-dimensional analysis of sloshing experiment is carried out using ALE finite element method in the commercial code LS-DYNA. The comparison of computational result and the experimental results is presented.

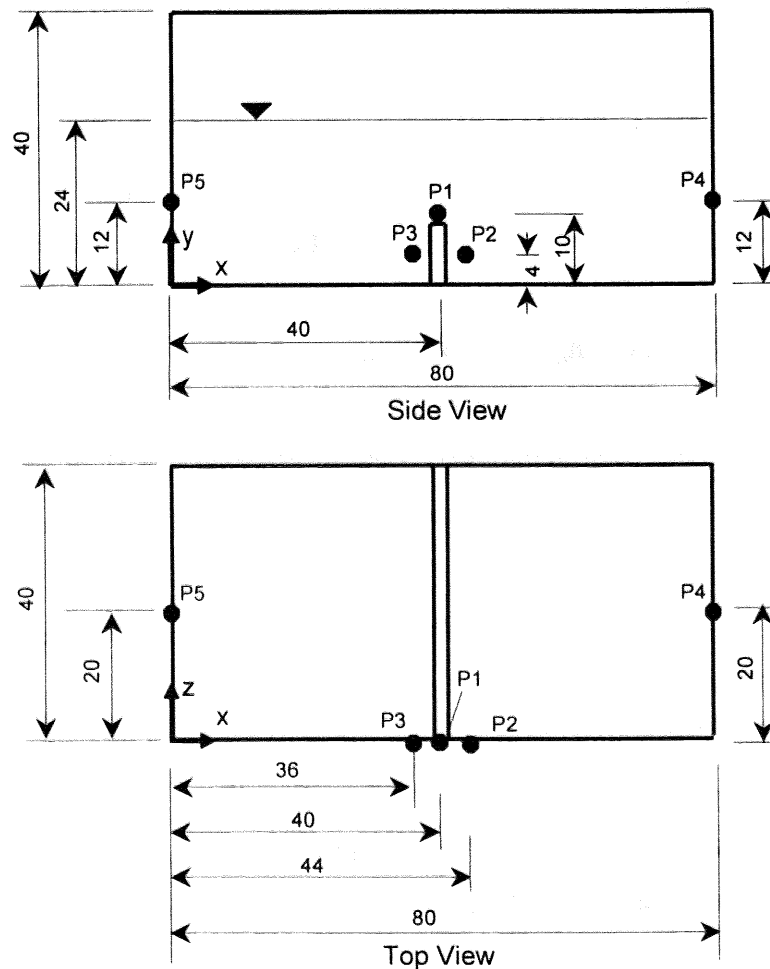


Fig. 5.1 Setup of rectangular tank

Figure 5.1 shows the setup of the rectangular tank sloshing experiment (Pierre C. Sames et al 2002). A rectangular tank at model scale with a fill level of 60% was used. The

tank was equipped with a baffle at the center of the bottom. Five sensors were located to measure time- dependent pressures. The size of the rectangular tank was 80 cm long, 40 cm wide and 40 cm deep.

Tank was excited with a harmonic horizontal motion (as shown in equation (5.1)) having an amplitude of $A_0 = 0.02 \text{ m}$ and a period of $T = T_N = 1.18 \text{ s}$, corresponding to the natural period of the fluid. Simulation time was set equal to $20 * T_N$, long enough to damp out the fluid motion after initial transients.

$$A = A_0 \sin\left(\frac{2\pi}{T}t\right) = 0.02 \sin\left(\frac{2\pi}{1.18}t\right) \quad 0 \text{ s} < t < 23.6 \text{ s} \quad (5.1)$$

The water is modeled as eight-node solid elements using the Constitutive Model & Equation of State. The dynamic viscosity and bulk modulus of water is $1.0038 \times 10^{-6} \text{ m}^2 / \text{s}$, $2.2 \times 10^9 \text{ N} / \text{m}^2$ respectively. Figure 5.2 shows the ALE FE mesh model for rectangular tank sloshing experiment.

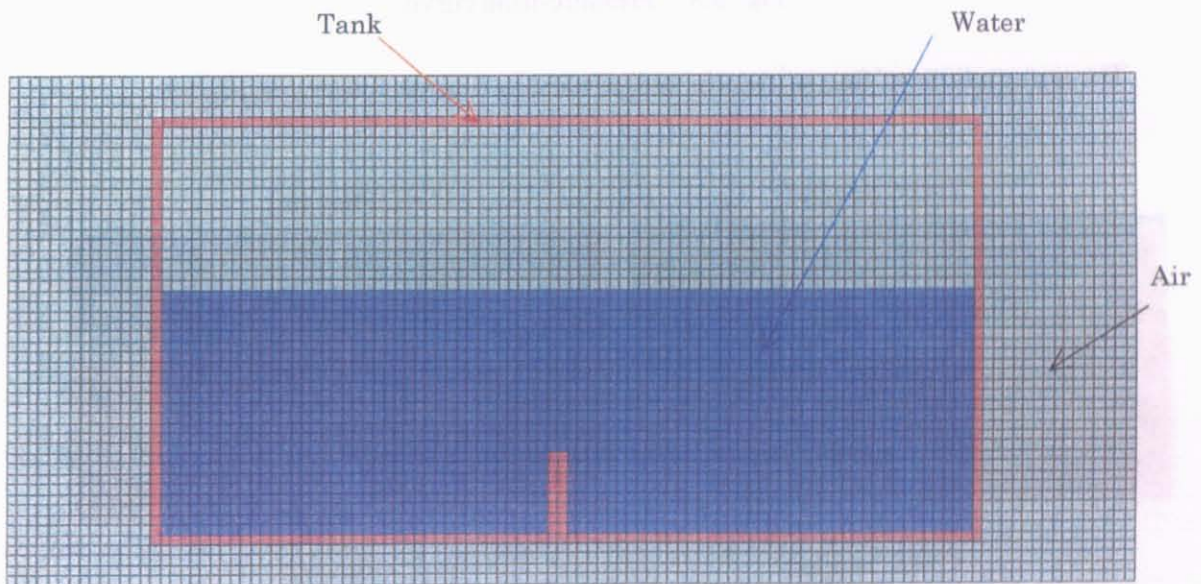


Fig. 5.2 ALE FE mesh model for sloshing experiment

Using ALE finite element method to analyze the rectangular tank sloshing experiment, the pressure signal computed and measured at location P4 are shown in Fig.5.3. Predicted pressure amplitudes were close to measurements after $T = 5 \text{ s}$. We believe that fluid-structure interaction of oil in tank can reliably be predicted by ALE FEM.

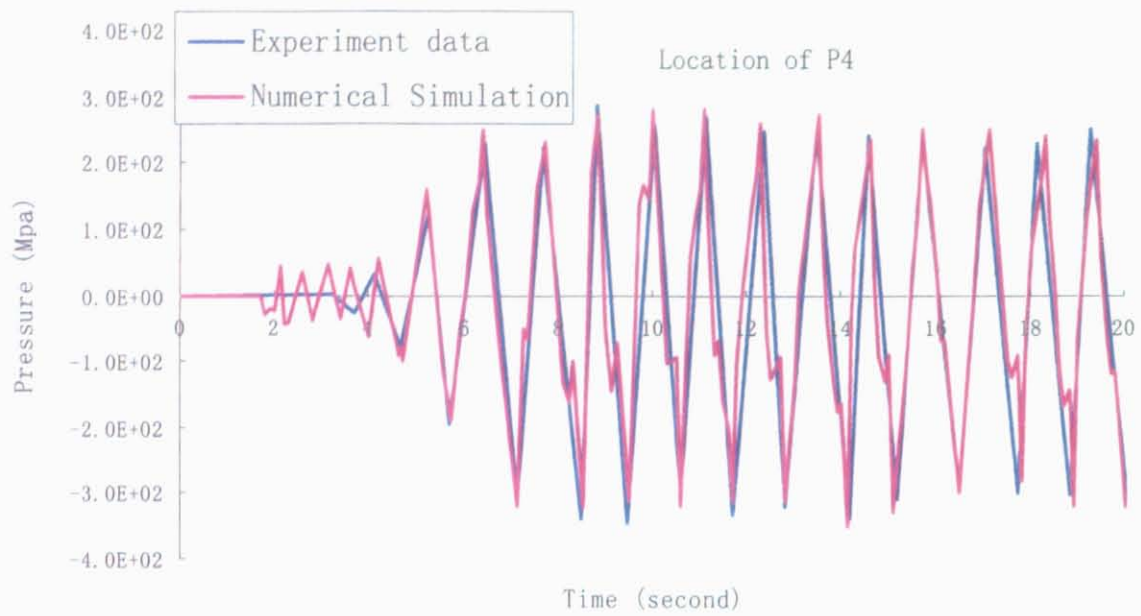


Fig. 5.3 Pressure-time curve

The deformation of free surface in tank at various time are plotted in Fig.5.4.

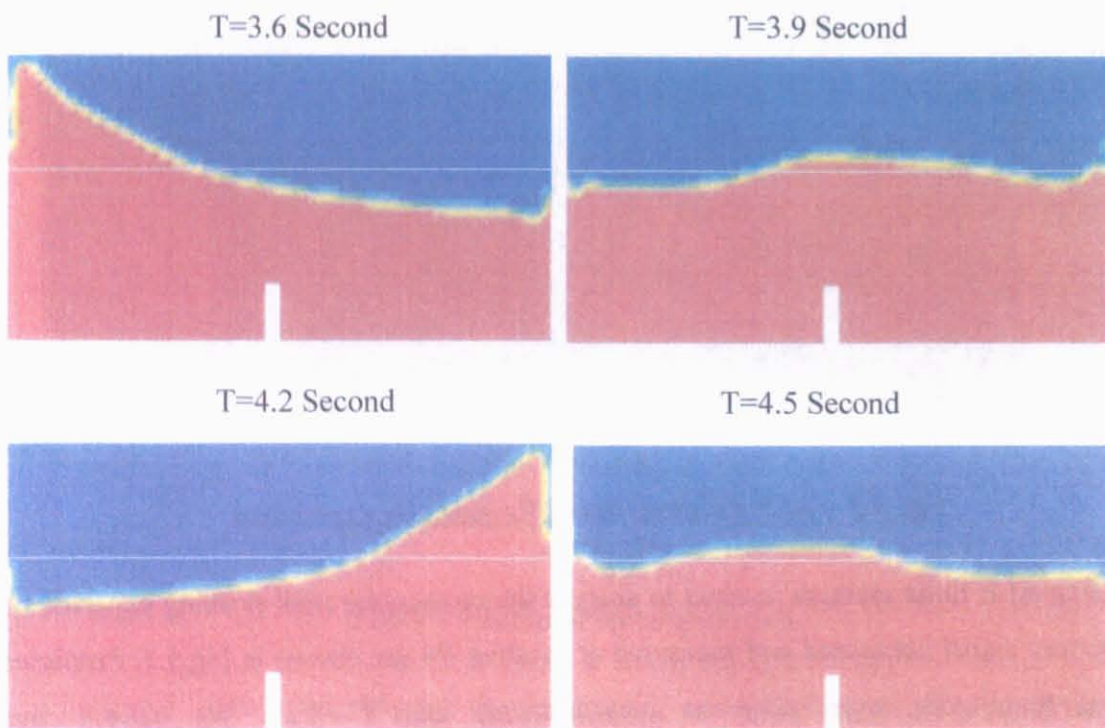


Fig. 5.4 Deformations of free surface at various times

5.3 Linear Sloshing Model for Fluid-structure Interaction of Liquid Cargo Tank

Tabri et al. (2004) treated the fluid-structure interaction in the ballast tank during ship collision as liquid sloshing and the sloshing effect is modelled by splitting the fluid mass into a part rigidly connected to the structure and the rest mass connected via a spring. In the following, the linear sloshing model to describe liquid sloshing is outlined.

Housner (1957) showed that the liquid hydrodynamic pressure in moving tank has two distinct components when the fluid is assumed to be incompressible and fluid displacement is assumed small. One component, known as impulsive pressure, is directly proportional to the acceleration of the tank. The second component is known as convective pressure and can be modelled by a mass-spring system.

- **Impulsive Pressure**

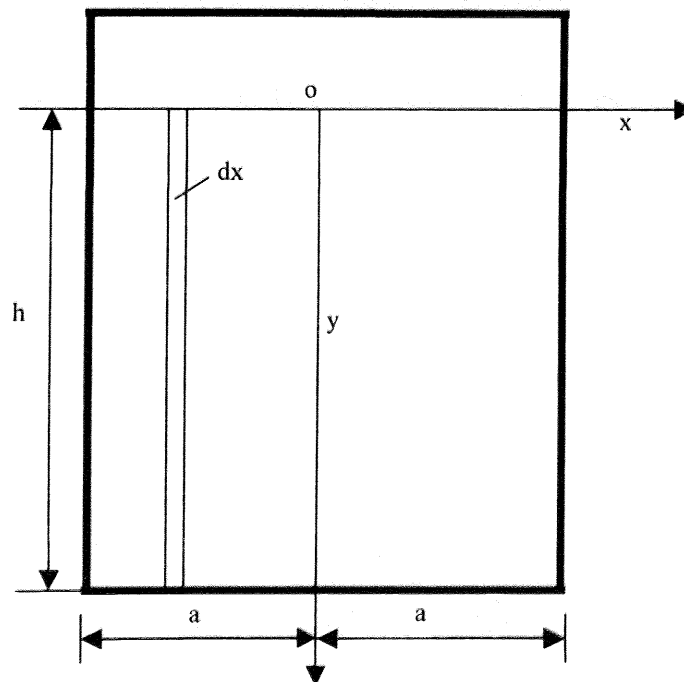


Fig. 5.5 Impulsive flow of fluid

Here we assume that the wall of container is given an impulsive acceleration \dot{u}_0 in the x direction and the fluid is constrained by thin, massless, vertical membranes. Then the fluid constrained between two adjacent membranes is given a vertical velocity

$$v = (h - y) \frac{du}{dx} \quad (5.2)$$

The accelerations satisfy the same equation, so

$$\dot{v} = (h - y) \frac{d\dot{u}}{dx} \quad (5.3)$$

The pressure in the fluid is then given by

$$p = \int_0^y -\rho(h - y) \frac{d\dot{u}}{dx} dy \quad (5.4)$$

The total horizontal force on one membrane is obtained by

$$P = \int_0^h p dy = -\frac{\rho h^3}{3} \frac{d\dot{u}}{dx} \quad (5.5)$$

The acceleration \dot{u} is determined from the horizontal motion of the fluid contained between two membranes. The equation of motion is given by

$$dP = -\rho h dx \cdot \dot{u} \quad (5.6)$$

Using the value of P from equation (5.5), the solution of \dot{u} is obtained by

$$\dot{u} = C_1 \cosh\left(\sqrt{3} \frac{x}{h}\right) + C_2 \sinh\left(\sqrt{3} \frac{x}{h}\right) \quad (5.7)$$

Using boundary condition

$$\dot{u} = \dot{u}_0 \quad \text{when } x = \pm a \quad (5.8)$$

The horizontal acceleration and pressure of fluid are given by

$$\dot{u} = \dot{u}_0 \cdot \frac{\cosh\left(\sqrt{3} \frac{x}{h}\right)}{\cosh\left(\sqrt{3} \frac{a}{h}\right)} \quad (5.9)$$

$$p = -\sqrt{3} \rho h \dot{u}_0 \left\{ \frac{y}{h} - \frac{1}{2} \left(\frac{y}{h} \right)^2 \right\} \frac{\sinh\left(\sqrt{3} \frac{x}{h}\right)}{\cosh\left(\sqrt{3} \frac{a}{h}\right)} \quad (5.10)$$

The pressure, force and moment on the wall and the bottom are obtained. It is seen that the over-all effect of the fluid on the walls of the container is the same as if a fraction of the total mass of the fluid were fastened rigidly to the walls of the container at a height above

the bottom. Based on an equivalent mechanical analogy, the magnitude of this equivalent mass, m_0 is given by

$$m_0 = \frac{2\rho h^2}{\sqrt{3}} \tanh\left(\frac{\sqrt{3}a}{h}\right) \quad (5.11)$$

Consider the total moment exerted on the wall and the bottom of the tank, the height of this equivalent mass, h_0 is obtained by

$$h_0 = \frac{3h}{8} \left(1 + \frac{4}{3} \left(\frac{\sqrt{3} \frac{a}{h}}{\tanh\left(\sqrt{3} \frac{a}{h}\right)} - 1 \right) \right) \quad (5.12)$$

● Convective Pressure

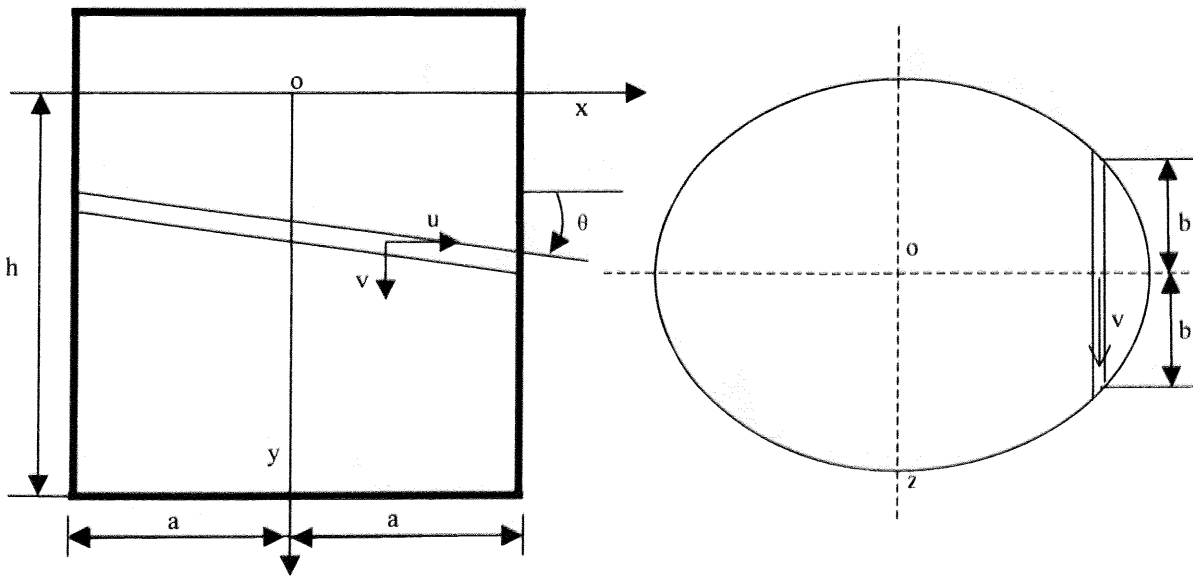


Fig. 5.6 Convective flow of fluid

u, v, w is the x, y, z components of convective fluid velocity respectively.

$$\left. \begin{aligned} \frac{\partial(ub)}{\partial x} &= -b \frac{\partial v}{\partial y} \\ v &= x\dot{\theta} \\ \frac{\partial u}{\partial x} + \frac{\partial v}{\partial y} + \frac{\partial w}{\partial z} &= 0 \end{aligned} \right\} \Rightarrow \left\{ \begin{aligned} u &= -\frac{1}{b} \cdot \frac{\partial \dot{\theta}}{\partial y} \int_{-a}^x x \cdot b dx \\ w &= z \cdot \frac{b'}{b^2} \cdot \frac{\partial \dot{\theta}}{\partial y} \int_{-a}^x x \cdot b dx \\ b' &= \frac{db}{dx} \end{aligned} \right. \quad (5.13)$$

Kinetic energy of fluid is given by

$$T = \frac{1}{2} \rho \int_0^h \int_{-a-b}^a \int_{-a}^b \left\{ x^2 \dot{\theta}^2 + \frac{1}{b^2} \cdot \left(\frac{\partial \dot{\theta}}{\partial y} \right)^2 \cdot \left(\int_{-a}^x x \cdot b dx \right)^2 \cdot \left(1 + z^2 \left(\frac{b'}{b} \right)^2 \right) \right\} dx dy dz \quad (5.14)$$

The potential energy of the fluid is given by

$$V = \frac{1}{2} \rho g \theta_h^2 \cdot \iint x^2 dx dz = \frac{1}{2} \rho g \theta_h^2 \cdot I_z \quad (5.15)$$

Since Hamilton Principle can be expressed as

$$\delta \int_{t_1}^{t_2} (T - V) dt = 0 \quad (5.16)$$

The solutions of θ, ω^2 are as follows

$$\begin{aligned} \theta &= \theta_h \cdot \frac{\sinh\left(\sqrt{\frac{5}{2}} \frac{y}{a}\right)}{\sinh\left(\sqrt{\frac{5}{2}} \frac{h}{a}\right)} \sin(\omega t) \\ \omega^2 &= \sqrt{\frac{5}{2}} \frac{g}{a} \tanh\left(\sqrt{\frac{5}{2}} \frac{h}{a}\right) \end{aligned} \quad (5.17)$$

The pressure in the fluid is given by

$$\begin{aligned} p &= -\rho \cdot \frac{\partial \ddot{\theta}}{\partial y} \left\{ -\int_{-a}^x \frac{Q}{b} dx + \frac{z^2}{2} \frac{b'}{b^2} Q \right\} \\ Q &= \int_{-a}^x b x dx \end{aligned} \quad (5.18)$$

The total force applied on the tank by the fluid is the same as would be produced by an equivalent mass m_1 that is spring mounted as shown in Fig.5.7. If m_1 oscillates with displacement x_1 , the force against the tank and the kinetic energy of the mass are as follows

$$\begin{aligned}
x_1 &= A_1 \sin \omega t \\
F_1 &= -m_1 A_1 \omega^2 \sin \omega t \\
T_1 &= \frac{1}{2} m_1 A_1^2 \omega^2 \sin^2 \omega t
\end{aligned} \tag{5.19}$$

The solutions of an equivalent mass m_1 is given by

$$m_1 = 2\rho a h b \cdot \left(\frac{1}{3} \sqrt{\frac{5}{2}} \frac{a}{h} \tanh \left(\sqrt{\frac{5}{2}} \frac{h}{a} \right) \right) \tag{5.20}$$

The stiffness of spring k_1 is given by

$$k_1 = 2\rho a h b \cdot \frac{5}{6} \frac{g}{h} \tanh^2 \left(\sqrt{\frac{5}{2}} \frac{h}{a} \right) \tag{5.21}$$

Considering the moment of the fluid pressure on the wall and the bottom, the height of this equivalent mass m_1 is obtained by

$$h_1 = h \cdot \left(1 - \frac{\cosh \left(\sqrt{\frac{5}{2}} \frac{h}{a} \right) - 2}{\sqrt{\frac{5}{2}} \frac{h}{a} \sinh \left(\sqrt{\frac{5}{2}} \frac{h}{a} \right)} \right) \tag{5.22}$$

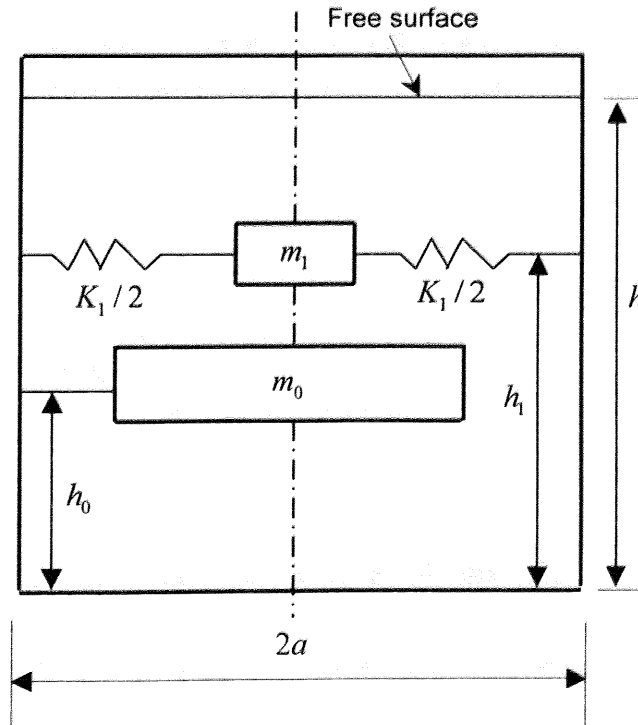


Fig. 5.7 Linear sloshing model

As shown in Fig.5.7, the over-all effect of the fluid upon the container is the same as a system consisting of a fixed mass m_0 and spring-mounted mass m_1 .

5.4 Ship Collision of Double Hull Oil Tanker

5.4.1 Scenario of Ship Collision

The ship collision between the bow of a 72,000 tonne oil tanker and a 293,000 tonne double hull VLCC is numerical simulated. The objective of this analysis is to study the effects of fluid in cargo tank on the motion and structural damage of struck ship in collision.

The principal dimensions of the striking ship and the struck ship are shown in Table 5.1. The midship cross-section and outline of struck ship are shown in Fig.5.8.

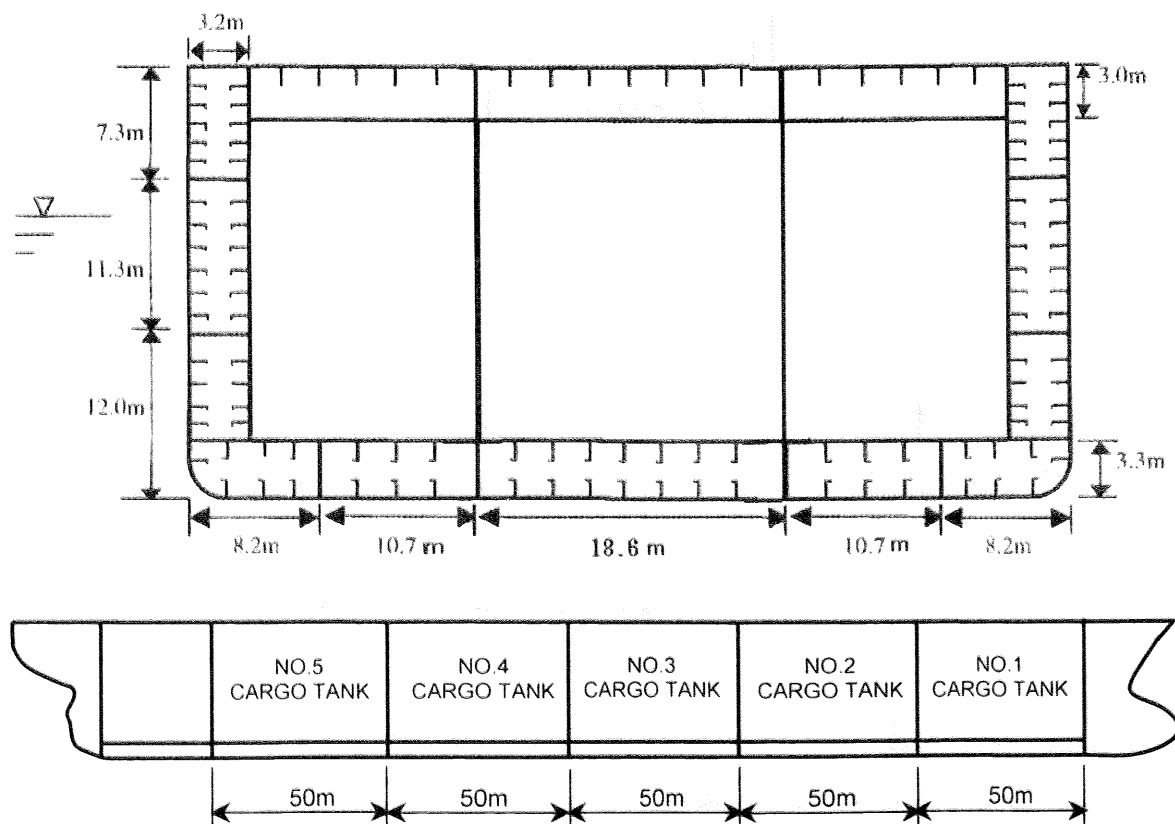


Fig. 5.8 Midship cross-section and outline of VLCC

Table 5.1 Principal dimensions of the striking ship and the struck ship

Parameter	The Striking Ship (Oil Tanker)	The Struck Ship (VLCC)
DWT(ton)	72,000	293,000
Length(m)	228.6	327.0
Breadth(m)	32.3	56.4
Depth(m)	20.2	30.6
Draught(m)	12.5	19.8
Sailing Velocity(m/s)	8	0

It is assumed that the striking ship sailing at a speed of 8m/s collide with the midship of VLCC at a right angle while the struck ship is at a standstill before collision. The typical filling level of the VLCC tank is greater than 95 percent of the tank height in the fully loaded condition. Here, 95 percent of high-filling level in fully loaded condition is considered.

5.4.2 Finite Element Modeling

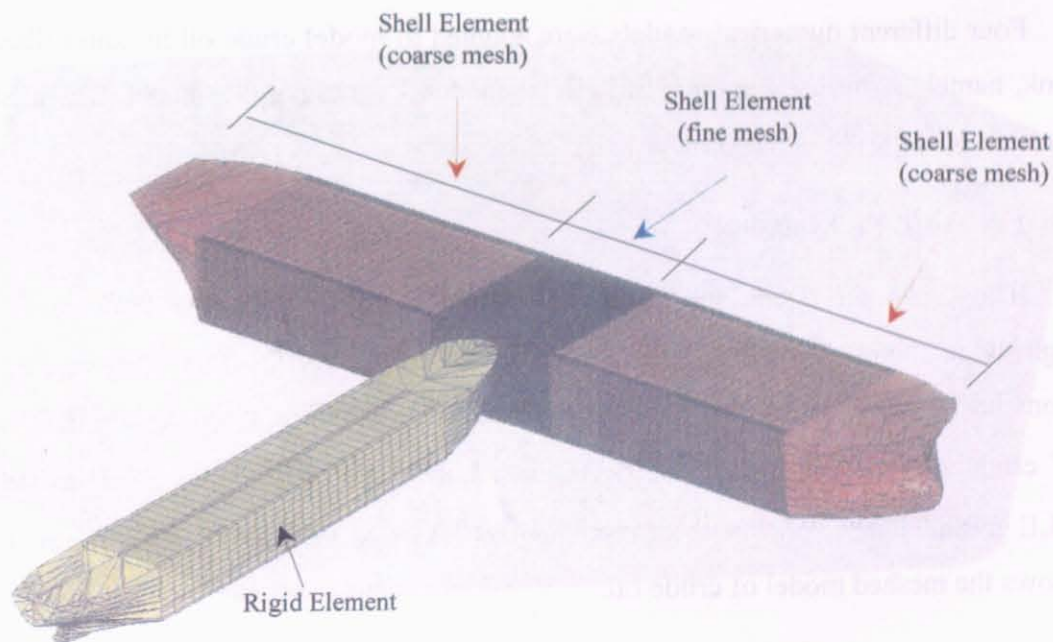


Fig. 5.9 FE modeling for ship collision

The computational finite element models were built using shell, solid and rigid elements as Fig. 5.9 shown. The striking ship is modelled as the rigid elements. The stuck ship(VLCC) constructed mild steel is modelled as plastic-elastic material, where the collision area(middle tank) is fine mesh($0.5m * 0.52m$ with 55214 shell elements) and other parts of struck ship is coarse mesh($1.6m * 2.5m$ with 23537 shell elements). The effect of all stiffeners and girders are taken as the equivalent plate thickness of hull shell in FE model. All structural members in the struck ship were assumed to be made in mild steel, with the material properties given in Table 5.2. The same simplified material model in Section 4.4.4, which uses the equations (4.2)-(4.4) to set up true stress-strain curve, was used. The surrounding water is modelled as point masses along the wetted area in FE model.

Table 5.2 Material property for struck ship model

Thickness (mm)	Yield Strength (MPa)	Ultimate Strength (MPa)	Experimental Rupture Strain	Young's Modulus (MPa)	Poisson Ratio
20	329	420	0.402	2.06×10^5	0.3

Four different numerical models were adopted to model crude oil in liquid filled cargo tank, namely Arbitrary Lagrangian Eulerian model, Lagrangian FE model, Linear Sloshing model and Rigid Point Mass model.

5.4.2.1 ALE FE Modeling

The crude oil inside the cargo tank and the void region are modeled as 55360 eight-node solid elements with $1.5m * 1.0m * 1.0m$ (ALE formulation) using the Constitutive Model & Equation of State. The density, dynamic viscosity and bulk modulus of crude oil is 860 kg/m^3 , $1.019 \times 10^{-5} \text{ m}^2/\text{s}$ and $1.455 \times 10^9 \text{ N/m}^2$, respectively. The ALE mesh motion follows the mass weighted average velocity in ALE mesh. Fig.5.10 shows the meshed model of crude oil.

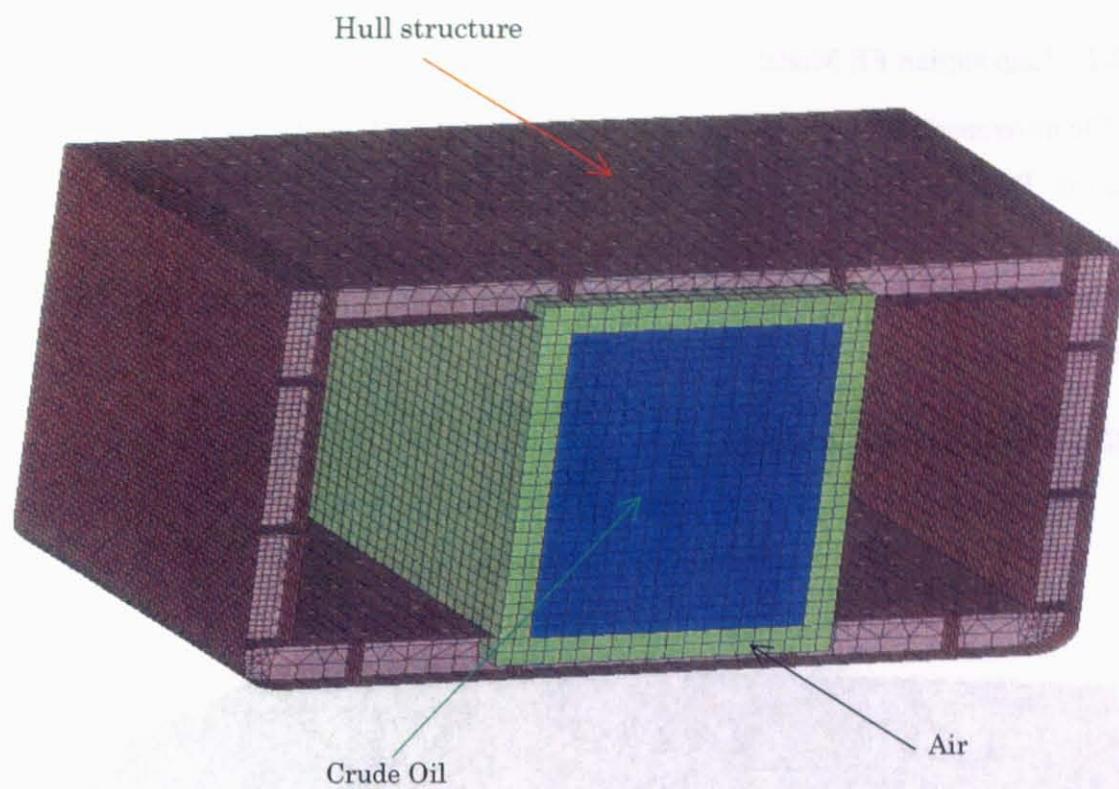


Fig. 5.10 Mesh of crude oil in ALE FE model

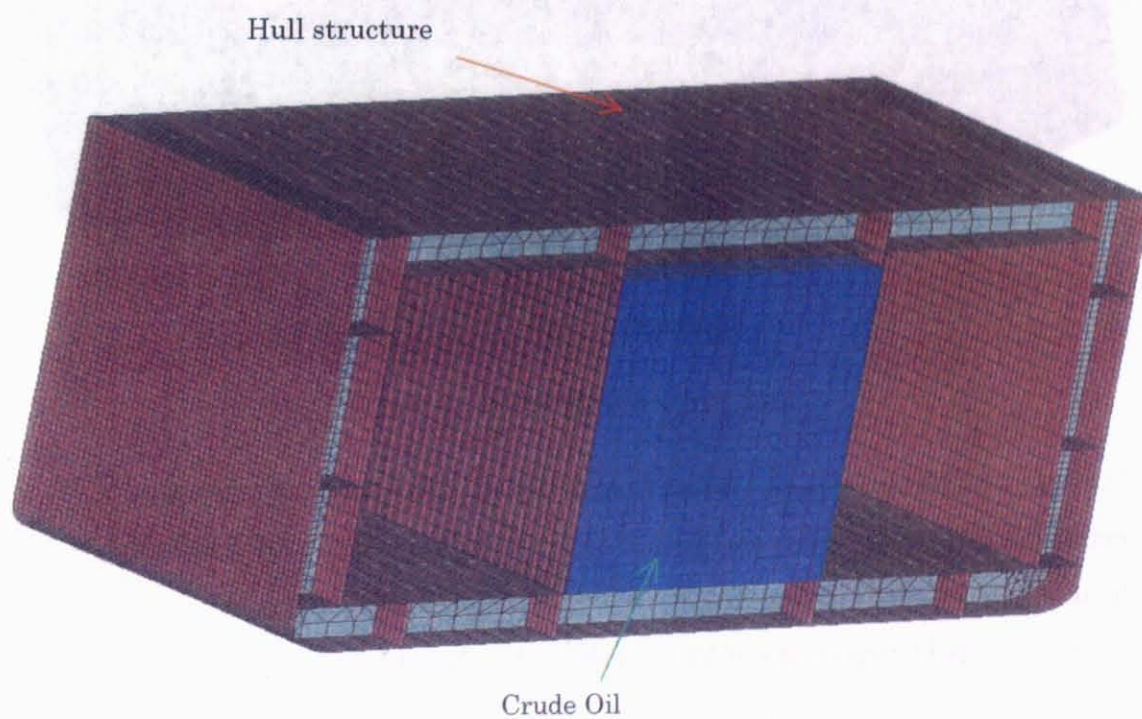


Fig. 5.11 Lagrangian FE model

5.4.2.2 Lagrangian FE Model

The difference between Lagrangian FE model and ALE FE model is how to model the crude oil. The crude oil in Lagrangian FE model is modelled as 41400 eight-node solid elements (Lagrangian formulation) with $1.5m \times 1.0m \times 1.0m$. The interaction between the crude oil and cargo tank is modelled using the contact algorithm where the crude oil was defined as slave part.

5.4.2.3 Linear Sloshing Modeling

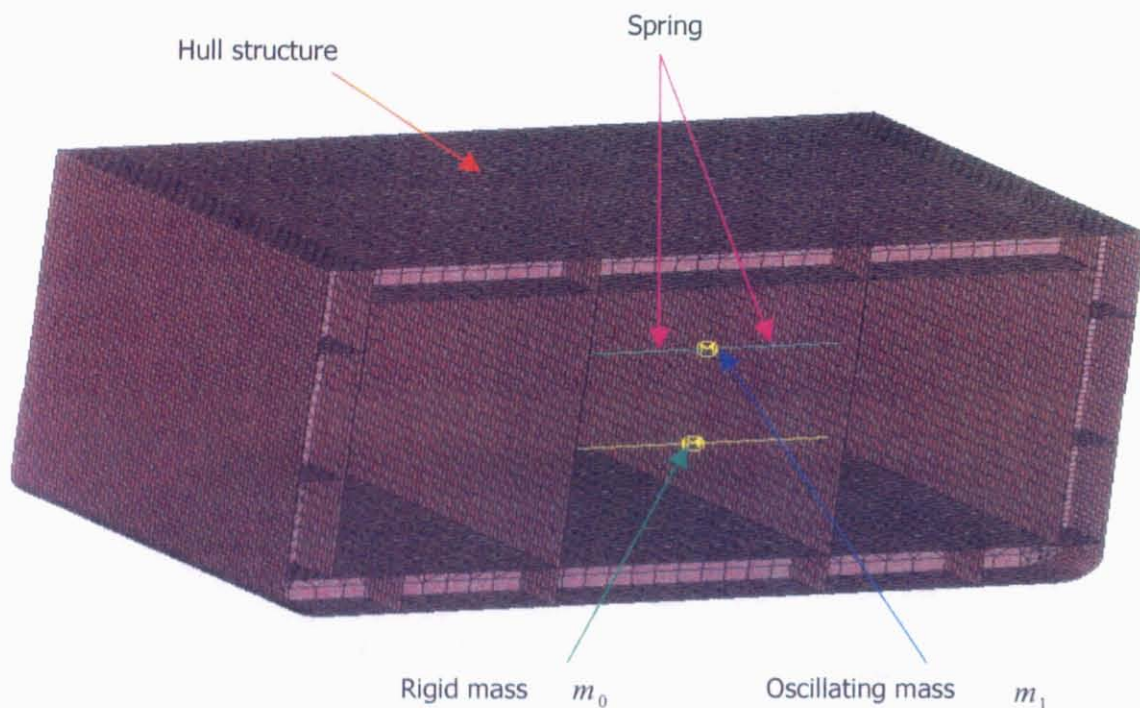


Fig. 5.12 Linear Sloshing Model

Using ALE finite element method to calculate the fluid-structure interaction needs long computational time. For convenience, it may be desirable to replace the fluid-structure interaction by Linear Sloshing Model.

For side liquid cargo tanks of VLCC in this case, $2a = 15.7\text{ m}$, $h = 23.2\text{ m}$, $b = 50\text{ m}$

The total mass of crude oil in side tanks(left tank and right tank) m_T is given by:

$$m_T = \rho \cdot 2a \cdot b \cdot h = 15662\text{ ton} \quad (5.23)$$

The equivalent masses (m_0 and m_1) in side tanks are given by:

$$m_0 = \frac{2\rho b h^2}{\sqrt{3}} \tanh\left(\frac{\sqrt{3}a}{h}\right) = 14085 \text{ ton} \quad (5.24)$$

$$m_1 = 2\rho a h b \cdot \left(\frac{1}{3} \sqrt{\frac{5}{2}} \frac{a}{h} \tanh\left(\sqrt{\frac{5}{2}} \frac{h}{a}\right)\right) = 2793 \text{ ton} \quad (5.25)$$

The equivalent heights (h_0 and h_1) in side tanks are given by:

$$h_0 = \frac{3h}{8} \left(1 + \frac{4}{3} \left(\frac{\sqrt{3} \frac{a}{h}}{\tanh\left(\sqrt{3} \frac{a}{h}\right)} - 1 \right) \right) = 10.00 \text{ m} \quad (5.26)$$

$$h_1 = h \cdot \left(1 - \frac{\cosh\left(\sqrt{\frac{5}{2}} \frac{h}{a}\right) - 2}{\sqrt{\frac{5}{2}} \frac{h}{a} \sinh\left(\sqrt{\frac{5}{2}} \frac{h}{a}\right)} \right) = 18.42 \text{ m} \quad (5.27)$$

The stiffness of spring in side tanks is given by:

$$k_1 = 2\rho a h b \cdot \frac{5}{6} \frac{g}{h} \tanh^2\left(\sqrt{\frac{5}{2}} \frac{h}{a}\right) = 5.517 \times 10^6 \text{ N/m} \quad (5.28)$$

For middle liquid cargo tank in midship of VLCC, $2a = 18.6 \text{ m}$, $h = 23.2 \text{ m}$, $b = 50 \text{ m}$

The total mass of crude oil in middle tank is given by:

$$m_T = 18555 \text{ ton} \quad (5.29)$$

The equivalent masses in middle tank are given by:

$$m_0 = 16055 \text{ ton} \quad m_1 = 3917 \text{ ton} \quad (5.30)$$

The equivalent heights (h_0 and h_1) in middle tank are given by:

$$h_0 = 10.51 \text{ m} \quad h_1 = 17.77 \text{ m} \quad (5.31)$$

The stiffness of spring in middle tank is given by:

$$k_1 = 6.529 \times 10^6 \text{ N/m} \quad (5.32)$$

5.4.2.4 Rigid Point Mass Modeling

For comparison with three FE models above mentioned, rigid point mass modelling is used to model the crude oil in liquid filled tank as rigid point masses. The struck ship FEM

model is consisting of shell elements attached to rigid point mass elements. The mass of rigid point mass elements is equal to the mass of crude oil in liquid cargo tank. The mass inertia moment of rigid point mass elements should be equivalent to that of real crude oil. For simple, we assume that the crude oil has the same movement as the struck ship and the fluid-structure interaction between the crude oil and tank structure is neglected in rigid point mass modeling. This modeling can decrease the CPU time significantly.

5.4.3 Results of Analysis

The results of four numerical models obtained after the simulations performed were compared. Main parameters include the contact force, the hydrodynamic force in liquid cargo tank, internal and kinetic energy of striking/struck ship.

The damage process of struck ship at different time using ALE FE model are shown in Fig.5.13. Figure 5.14, 5.15, 5.16 and 5.17 show the progressive damage process of struck cargo tank for ALE Model, Lagrange Model, Linear Sloshing model and Rigid Point Mass Model when the rupture of outer shell and inner shell happened, respectively. When reviewing the *progressive damage process* for 4 different models, the numerical simulation results of ALE Model and Lagrange Model compare well with regards to the damage behaviour for the rupture of outer shell and inner shell. All of four different FE Models predict almost the same outer shell structure rupture time (0.22 second). However, the time of inner shell structure rupture for Linear Sloshing model and Rigid Point Mass Model is at 0.648second, 0.684 second, respectively, which is much later than those of ALE FE Model (0.572 second) and Lagrange FE Model (0.558 second). This means that linear sloshing model and rigid point mass model overestimate the crashworthiness of VLCC side structure and the capability of absorbed internal energy when the rupture of the inner shell structure happened.

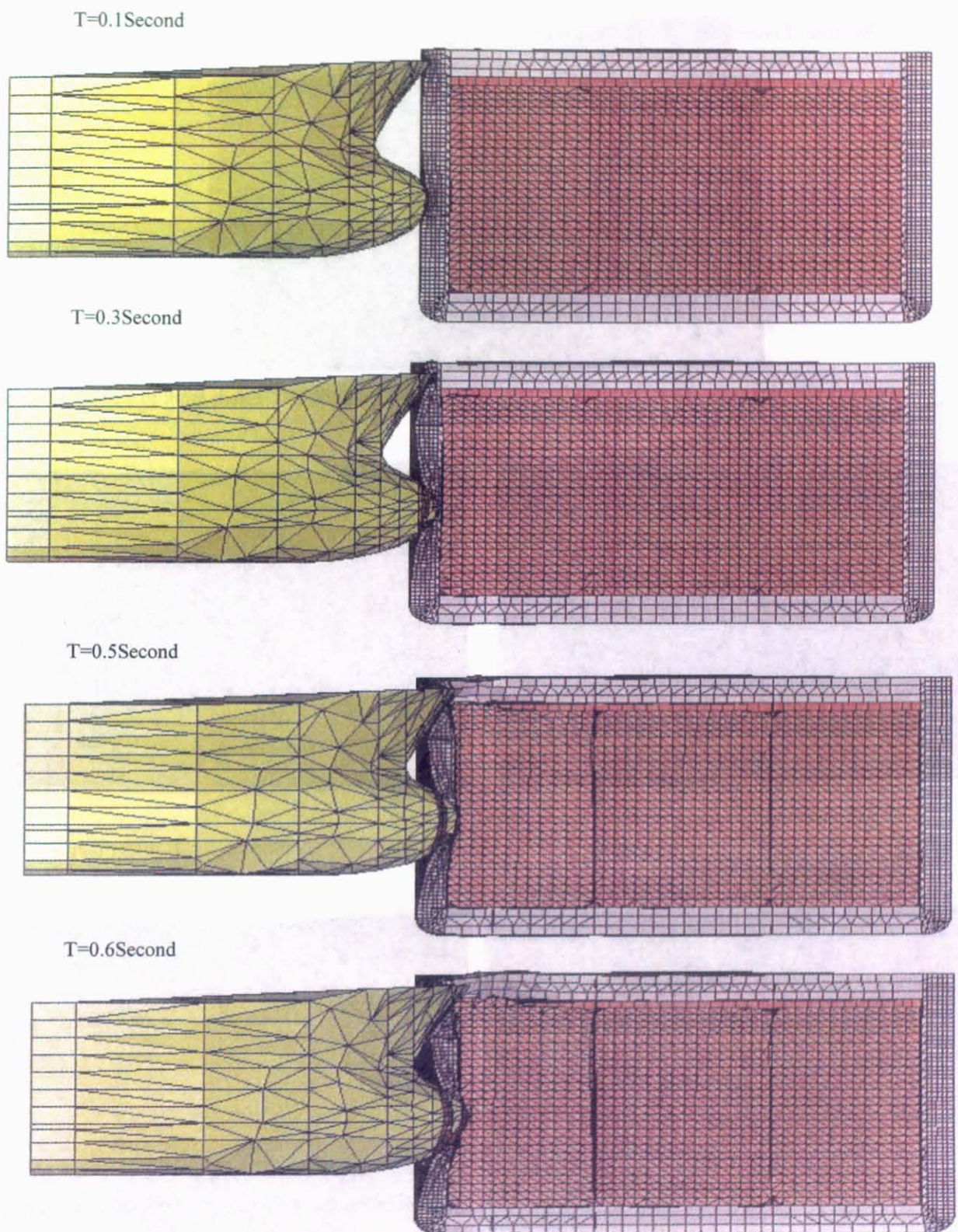
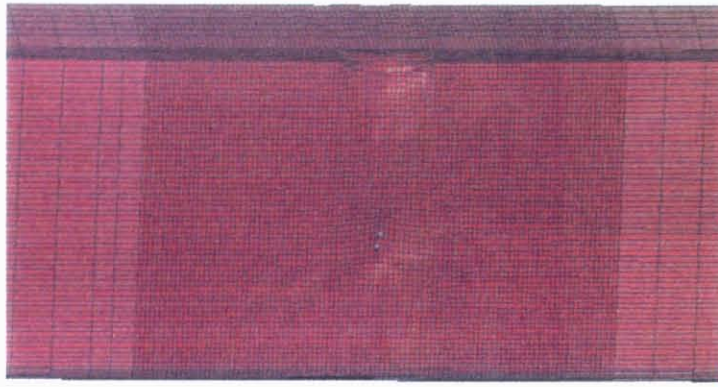
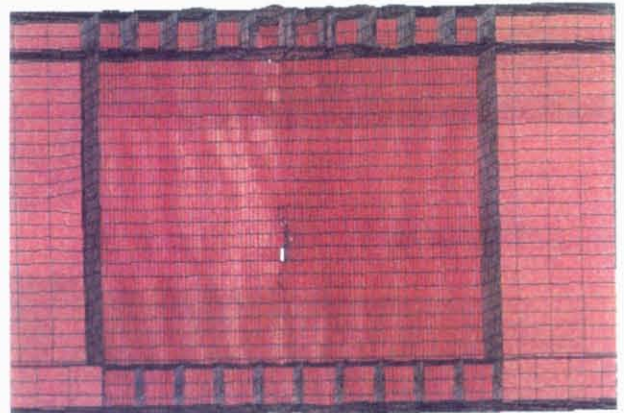
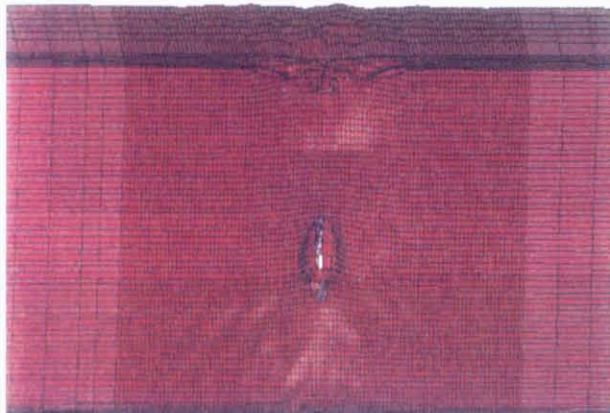


Fig. 5.13 The deformation of struck ship at different time for ALE FE Model

Rupture of outer shell $T=0.21$ Second



Rupture of inner shell $T=0.572$ Second



$T=0.6$ Second

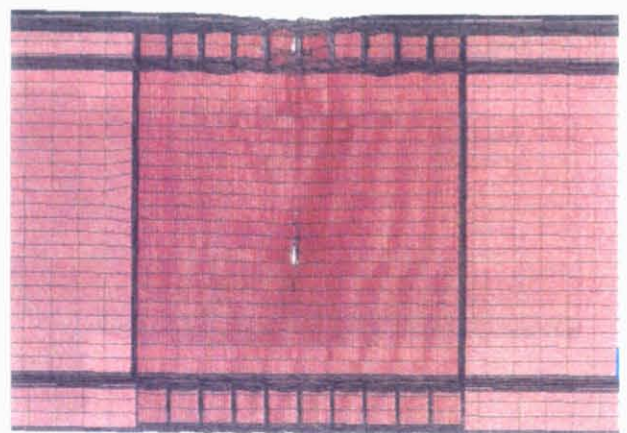
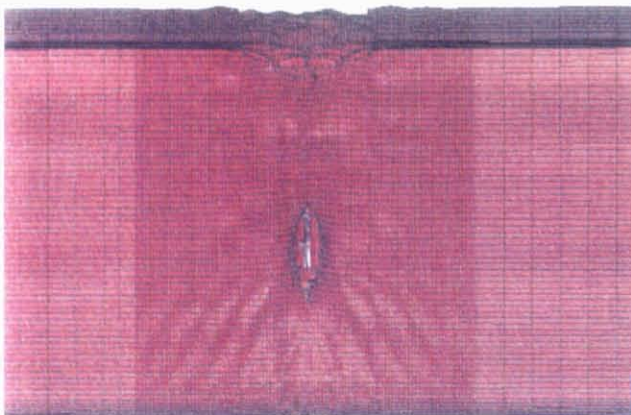
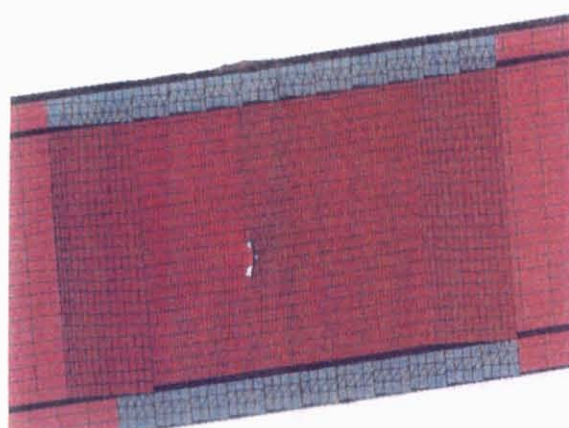


Fig. 5.14 Damages to side structures at different time for ALE FE Model

Rupture of outer shell $T=0.216$ Second



Rupture of inner shell $T=0.558$ Second



$T=0.7$ Second

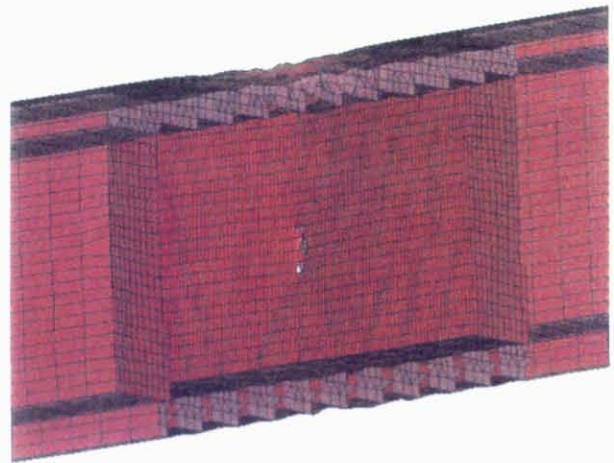


Fig. 5.15 Damages to side structures at different time for Lagrange FE Model

Rupture of outer shell $T=0.22$ Second



Rupture of inner shell $T=0.648$ Second



$T=0.8$ Second



Fig. 5.16 Damages to side structures at different time for Linear Sloshing Model

Rupture of outer shell $T=0.22$ Second



Rupture of inner shell $T=0.684$ Second



$T=1.0$ Second

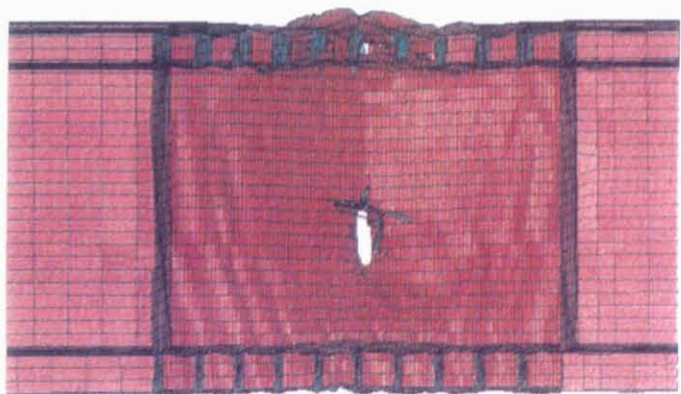
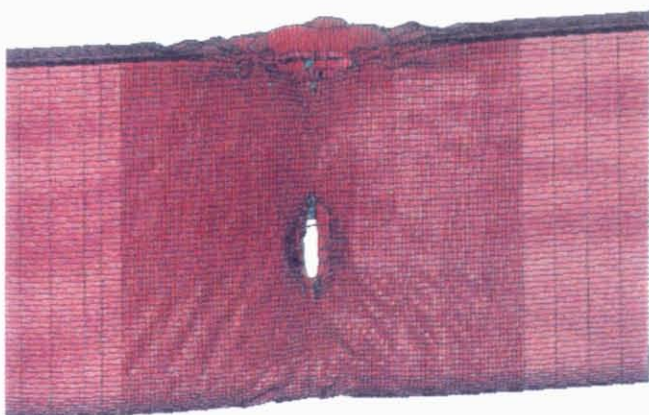


Fig. 5.17 Damages to side structures at different time for Rigid Point Mass Model

5.4.3.1 The Internal Energy of Struck Ship

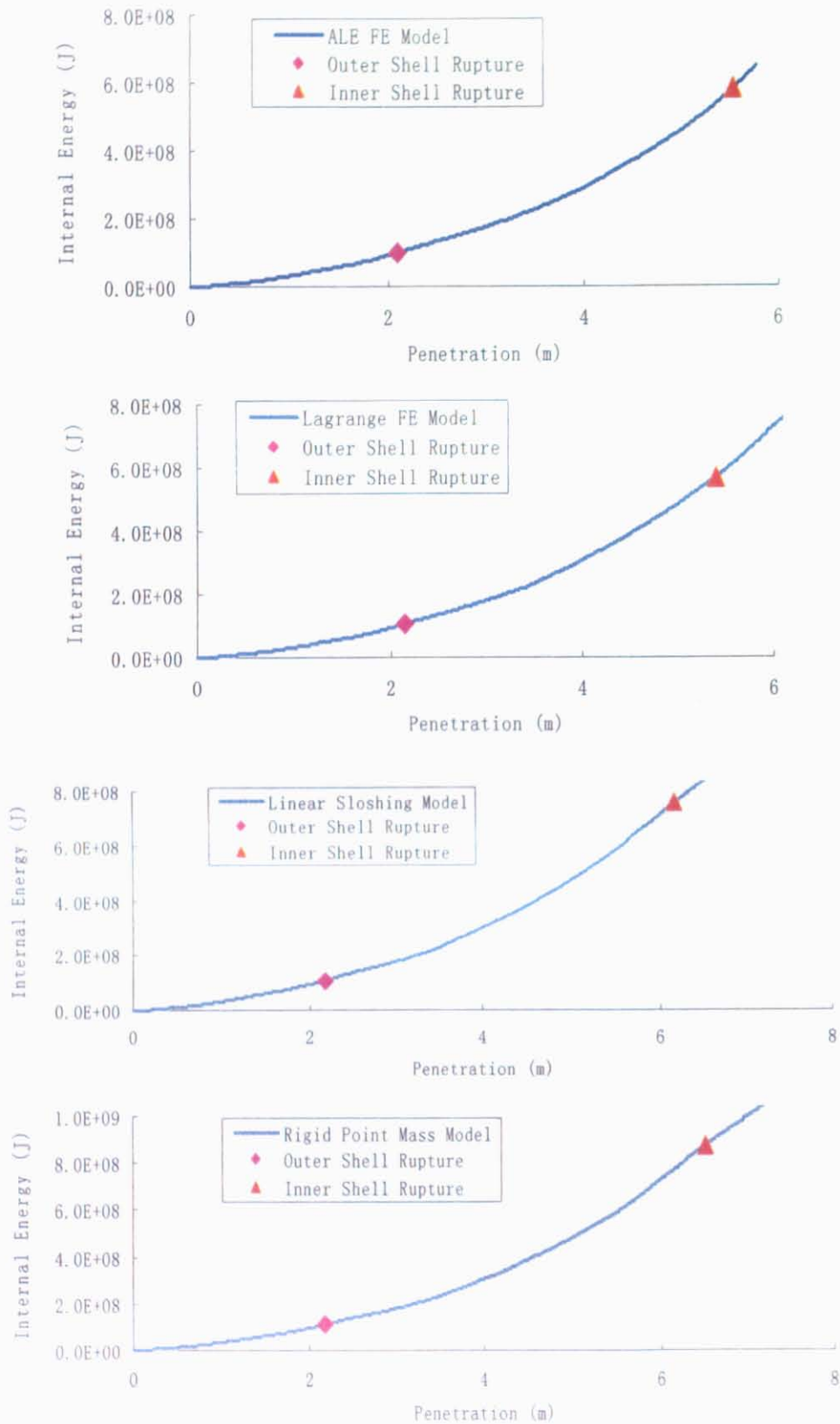


Fig. 5.18 Internal energy-penetration curves of struck ship

The absorbed internal energy-penetration curves of struck ship for different models are presented in Fig.5.18. When reviewing the plots, all of four different FE models predict almost the same absorbed internal energy (110 MJ) when outer shell structure rupture happened. However, when the rupture of inner shell structure occurred, the absorbed internal energy for Rigid Point Mass Model is 875 MJ, which is much larger than those of ALE FE Model (580 MJ) and Lagrange FE Model (569 MJ). This means that rigid point mass model overestimate the absorbed internal energy of VLCC when the rupture of the inner shell structure happened. The results of ALE FE model and Lagrangian FE model were compared well. At the rupture time of inner shell, the rigid point mass model will overestimate 50.9% absorbed energy of struck ship compared with the results of ALE FE model.

5.4.3.2 The Impact Force Curve between the Bow and the Struck Ship

The impact force-penetration curves of struck ship for different models are presented in Fig.5.19. Since the crude oil cargo tank is a double-hull tank, the effect of fluid-structure interaction of liquid filled tank on the impact force between the bow and the struck cargo is relatively small. When the rupture of the outer shell and inner shell occurred, the impact force is very similar for four different FE Models. At the rupture time of inner shell, the difference of the impact force between rigid point mass model and ALE FE model is only 3.32%.

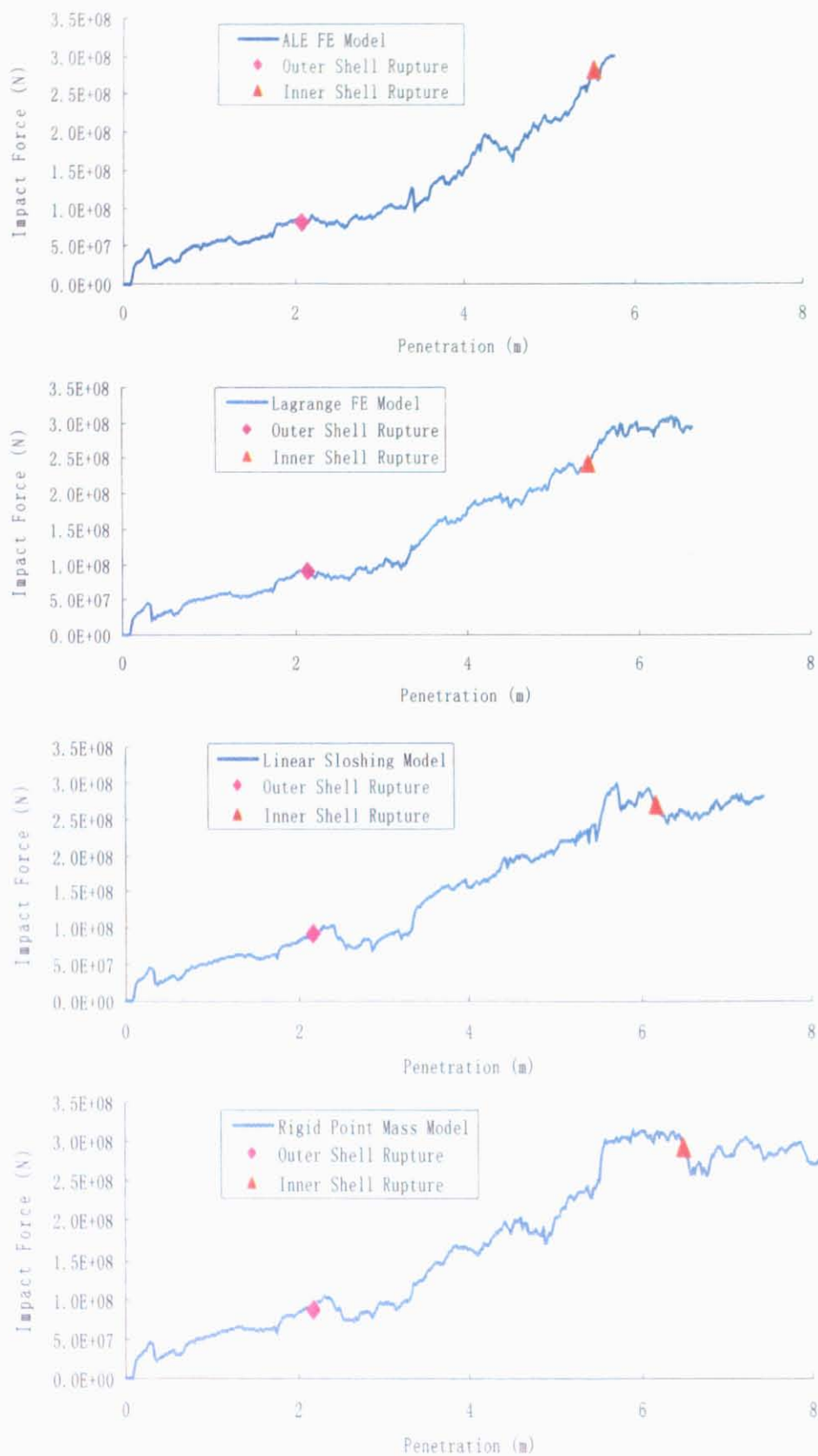


Fig. 5.19 Impact force-time curves for different FE Model

5.4.3.3 Hydrodynamic Force in Liquid Filled Cargo Tank

The predicted hydrodynamic forces in three liquid filled cargo tanks for ALE FE model, Lagrangian FE model and Linear Sloshing model are shown in Fig.5.20, 5.21 and 5.22. The comparison of hydrodynamic forces in left, middle and right liquid tank for ALE FE model, Lagrangian FE model and Linear Sloshing model is shown in Fig.5.23, 5.24 and 5.25, respectively. Figures 5.20, 5.21 and 5.22 show that the hydrodynamic force in left liquid tank, which is near to the struck side structure, is much larger than the one in middle and right liquid tank. The fluid-structure interaction in middle and right liquid tank is small. This means that the contribution of liquid cargo in middle and right tank is small. Neglecting these parts of fluid-structure interaction may not induce big numerical simulation error. We can model the crude oil in middle and right liquid tank as rigid point mass instead of ALE element to reduce the calculation time. Both ALE FE model and Lagrangian FE model predict similar hydrodynamic force in the left liquid tank. Both ALE FE model and Lagrangian FE model can accurately simulate the fluid-structure interaction of liquid cargo in tank.

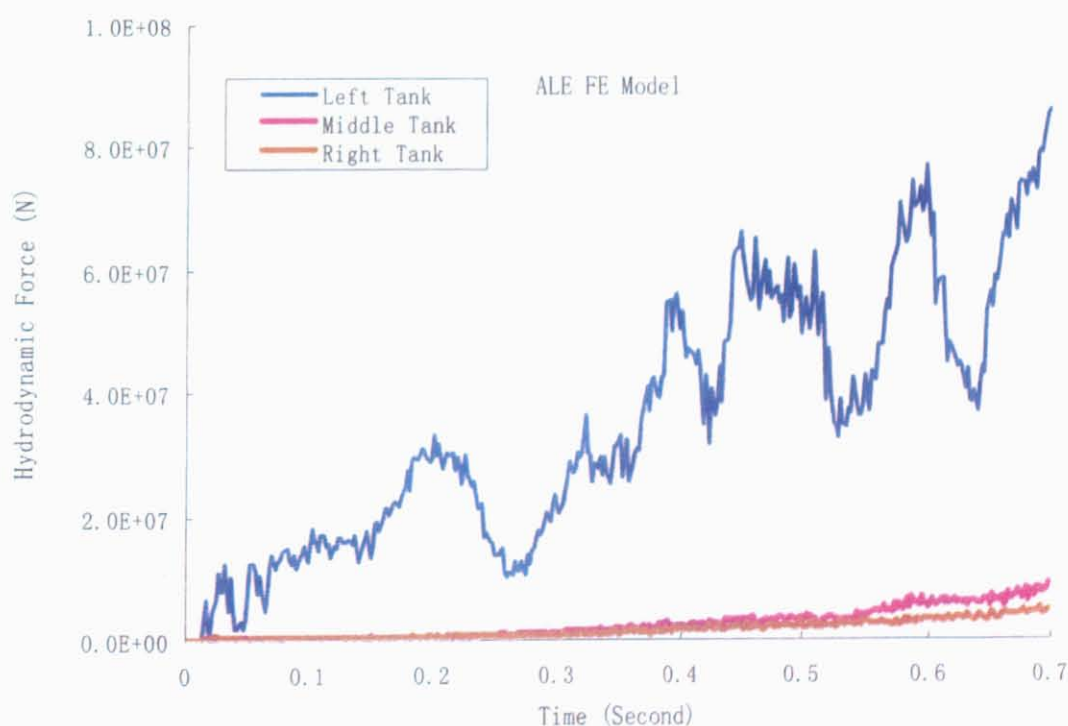


Fig. 5.20 Hydrodynamic forces for ALE FE model

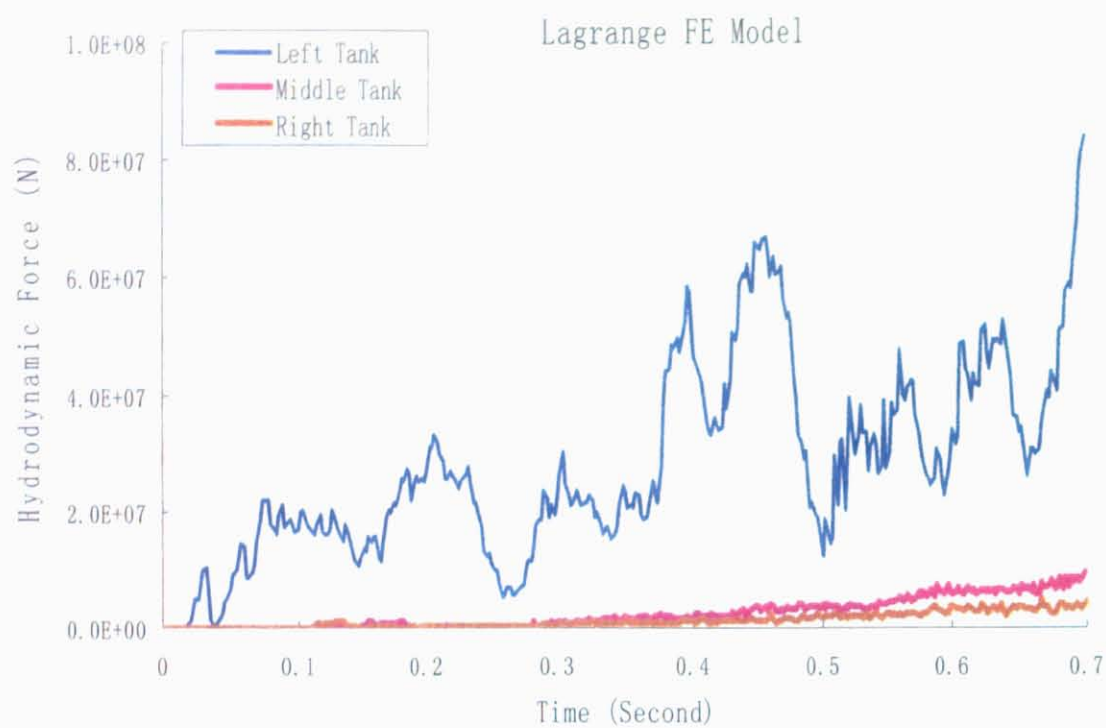


Fig. 5.21 Hydrodynamic forces for Lagrangian FE model

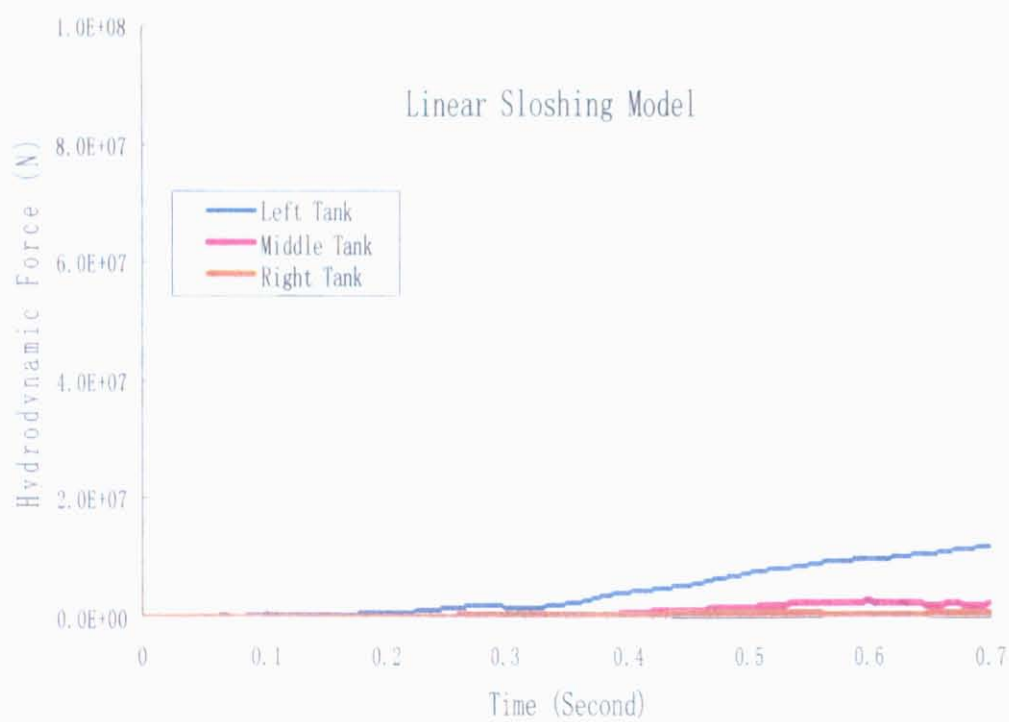


Fig. 5.22 Hydrodynamic forces for Linear Sloshing model

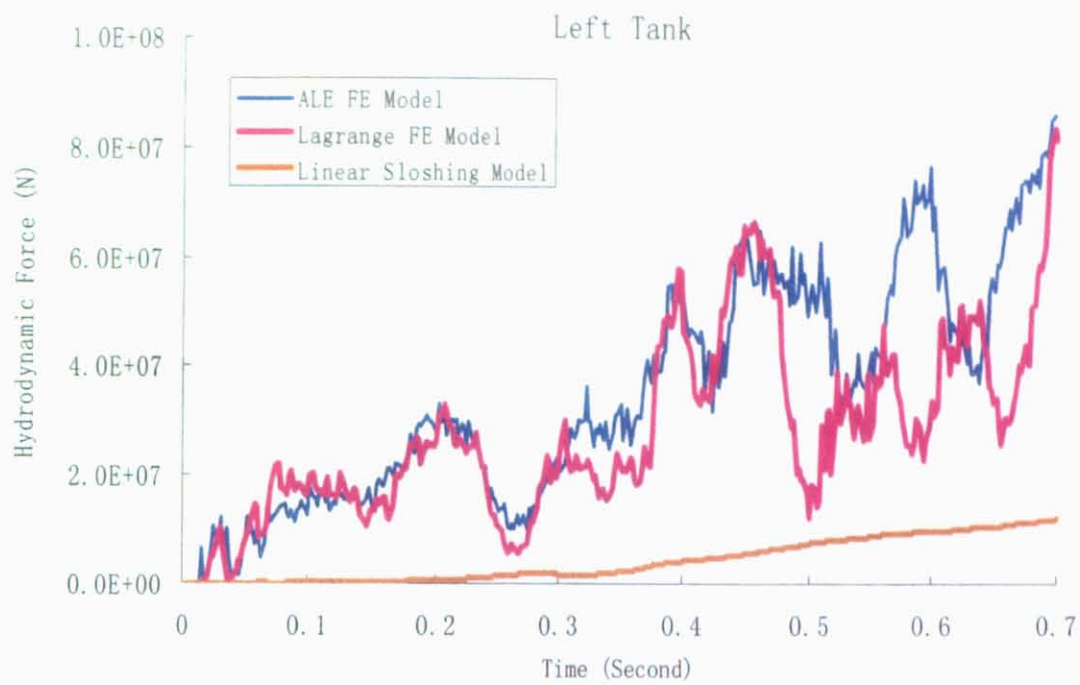


Fig. 5.23 Hydrodynamic forces in left tank

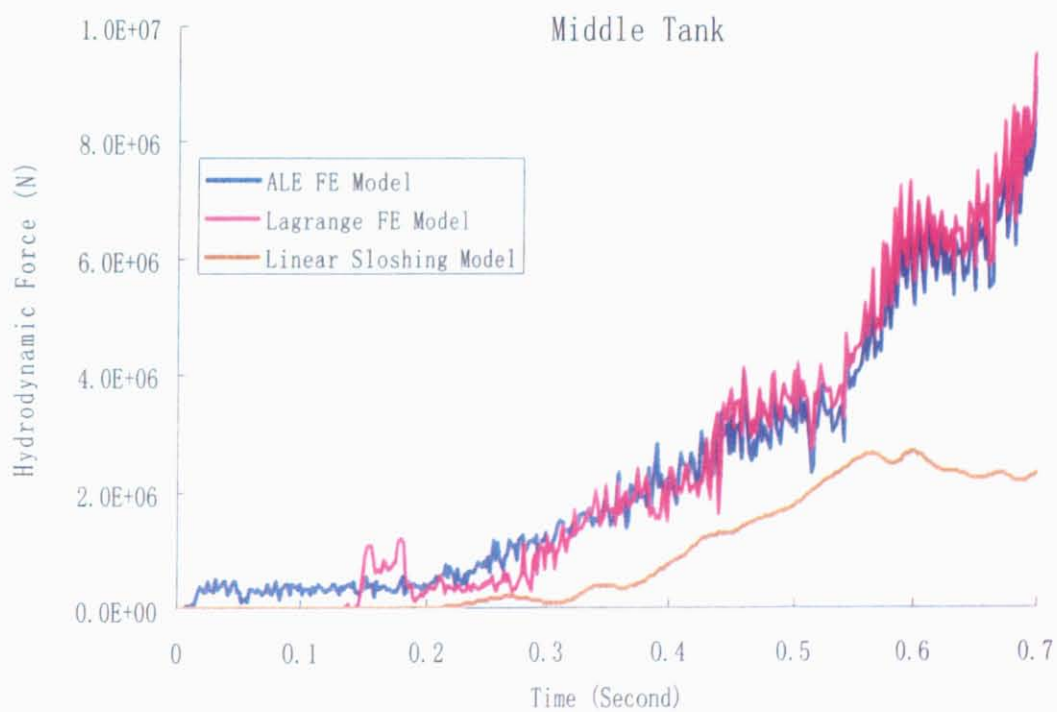


Fig. 5.24 Hydrodynamic forces in middle tank

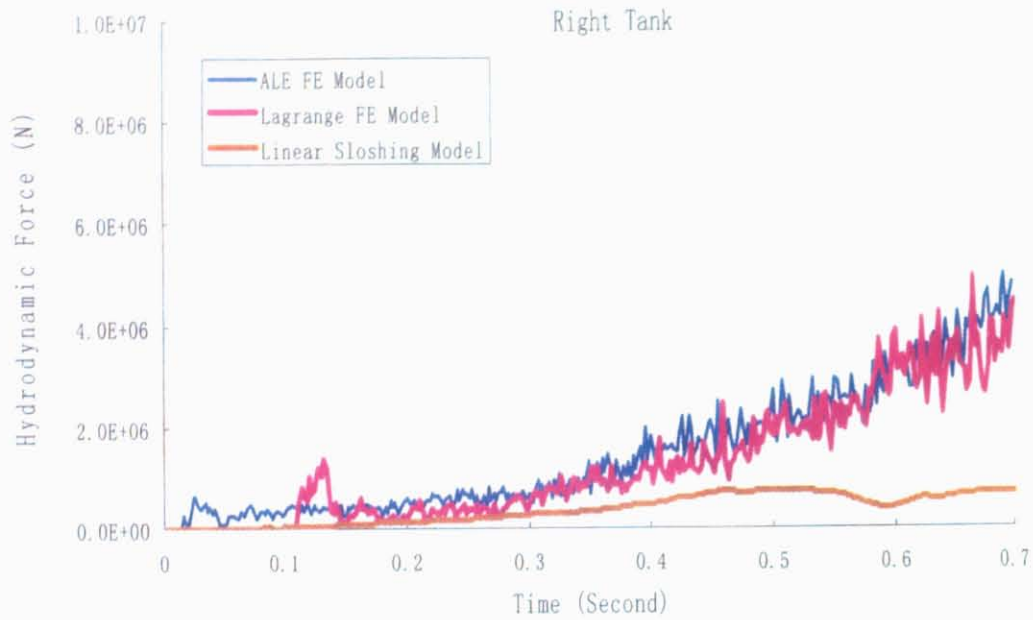


Fig. 5.25 Hydrodynamic forces in right tank

Main parameters including penetration, the impact force, velocity of striking ship along collision direction, kinetic energy of struck ship, absorbed internal energy at the time of rupture of inner shell are presented in Table 5.2. The CPU time for four numerical models is also presented in Table 5.2

Table 5.2 Main parameters at rupture time of inner shell

	ALE FE Model	Lagrangian FE Model	Linear Sloshing Model	Rigid Point Mass Model
Time of inner shell rupture(s)	0.572	0.558	0.648	0.684
Penetration(m)	5.52	5.39	6.17	6.50
The impact force (MN)	283	244	270	293
Velocity of Striking ship(m/s)	9.11	9.12	8.82	8.64
Kinetic energy of struck ship(MJ)	44	41	59	95
Absorbed energy by ship collision (MJ)	579	569	755	875
CPU time	16 hrs 32 mins	4hrs 17 mins	3hrs 47 mins	4hrs 44 mins

5.5 Remarks

In this chapter, the ALE finite element method is validated by the rectangular tank sloshing experiment. Four different numerical FE models for liquid cargo in tank were used to numerical analysis the ship collision between a 72,000 tonne tanker and a 293,000 tonne double hull VLCC. The advantage of ALE FE method is that it can accurately simulate the fluid-structure interaction in liquid cargo tank. However the CPU time of this method is much larger than other three FE models. On the other hand, although the Linear Sloshing FE model and Rigid Point Mass model need the shortest CPU time, these FE model underestimate the hydrodynamic force in liquid cargo tank. The Linear Sloshing FE model and Rigid Point Mass model also predict the different structure damage compared with the results of ALE Model and Lagrange Model. Compared to the result of ALE FE model, the Lagrangian FE model is appropriate for predicting the critical striking velocity and the structure behaviour of damaged struck cargo tank accounting for the fluid-structure interaction in liquid cargo tank with reasonable accurateness and a relatively low required CPU time.